

Topological Engineering of a Frustrated Antiferromagnetic Triradical in Aza-Triangulene Architectures

Francisco Romero-Lara,^{1,*} Manuel Vilas-Varela,^{2,*} Ricardo Ortiz,^{3,4,*} Manish Kumar,⁵ Alessio Vegliante,¹ Lucía Gómez-Rodrigo,² Jan Patrick Calupitan,^{3,6,7} Diego Soler,⁵ Nikas Friedrich,¹ Dongfei Wang,^{1,8} Jon Ortuzar,¹ Stefano Trivini,¹ Fabian Schulz,¹ Thomas Frederiksen,^{3,9} Pavel Jelínek,⁵ Diego Peña,^{2,10,†} and José Ignacio Pascual^{1,9,‡}

¹CIC nanoGUNE-BRTA, 20018 Donostia-San Sebastián, Spain

²Centro Singular de Investigación en Química Biolóxica e Materiais Moleculares (CiQUS) and Departamento de Química Orgánica, Universidad de Santiago de Compostela, 15782 Santiago de Compostela, Spain

³Donostia International Physics Center (DIPC), 20018 Donostia-San Sebastian, Spain

⁴CICECO- Aveiro Institute of Materials, Department of Chemistry, University of Aveiro, 3810-193 Aveiro, Portugal

⁵Institute of Physics of the Czech Academy of Sciences, Cukrovarnická 10, Prague 6, CZ 16200, Czech Republic

⁶Centro de Física de Materiales (CFM-MPC), Centro Mixto CSIC-UPV/EHU, E-20018 Donostia-San Sebastián, Spain

⁷Sorbonne Université, CNRS, Institut Parisien de Chimie Moléculaire (IPCM), F-75005 Paris, France

⁸School of Physics; Centre for Quantum Physics, Beijing Institute of Technology, 100081 Beijing, China

⁹Ikerbasque, Basque Foundation for Science, 48009 Bilbao, Spain

¹⁰Oportunius, Galician Innovation Agency (GAIN), 15702 Santiago de Compostela, Spain

(Dated: December 12, 2025)

Open-shell nanographenes provide a versatile platform to host unconventional magnetic states within their π -conjugated networks. Particularly appealing are graphene architectures that incorporate spatially separated radicals and tunable interactions, offering a scalable route toward spin-based quantum architectures. Triangulenes are ideal for this purpose, as their radical count scales with size, although strong hybridization prevents individual spin control. Here, we realize a radical reconfiguration strategy that transforms a single-radical aza-triangulene into a frustrated antiferromagnetic triradical by covalently extending it with armchair anthene moieties of increasing length. Scanning tunnelling spectroscopy reveals edge-localized Kondo resonances and a doublet-to-quartet spin excitation, evidencing the emergence of correlated spins. Multi-reference electronic-structure calculations trace the progressive increase in polyyradical character with anthene length, driven by the clustering of frontier states within a narrow energy window. Consequently, the initial single-radical doublet reorganizes into a frustrated triradical with weakly coupled edge spins, a molecular analog of a three-qubit quantum register.

Open-shell nanographenes provide a chemically precise route to engineer spin arrays for quantum information technologies. Their π -conjugated lattices can host spatially separated electronic spins that are naturally protected from decoherence thanks to weak spin-orbit and hyperfine couplings [1–5]. The possibility of encoding and coherently manipulating such spin states makes nanographenes attractive building blocks for molecular quantum registers [6].

Triangulene represents one of the most prototypical open-shell polycyclic aromatic hydrocarbons (PAHs) due to its non-Kekulé structure and a spin ground state that correlates directly with its size [7]. Recent advances in on-surface synthesis [8] have enabled the successful fabrication of triangulenes [9–13], targeting spin-state control through molecular size and the design of covalently linked architectures [14–23]. In triangulenes, all radical centers reside on the same sublattice, leading to strong wavefunction overlap and ferromagnetic-like exchange interactions that maximize the total spin, in accordance with Lieb’s

theorem [24, 25].

Introducing antiferromagnetic exchange pathways between conjugated spins opens new opportunities to induce frustration within the π -network [26–29], thereby favoring entangled spin states in the ground state. A particularly effective strategy to achieve this involves substitutional doping, which modifies the sublattice symmetry, the spin ground state, and their exchange interactions without disrupting the conjugated framework of the nanographene [30–35]. For instance, replacing the central carbon of a [3]-triangulene with nitrogen, i.e. in aza-[3]-triangulene (**AT**), introduces an additional π -electron into the majority-spin manifold. While this configuration might naively be expected to stabilize a high-spin triradical state, in practice the extra electron occupies the pair of degenerate zero-energy states (ZES) of the [3]-triangulene, resulting in a single radical and spin-doublet ground state (Fig. 1) that is further stabilized by a Jahn-Teller distortion [30, 36].

Here, we present a strategy for transforming the spin-doublet **AT** molecule [30, 36] into a triradical platform

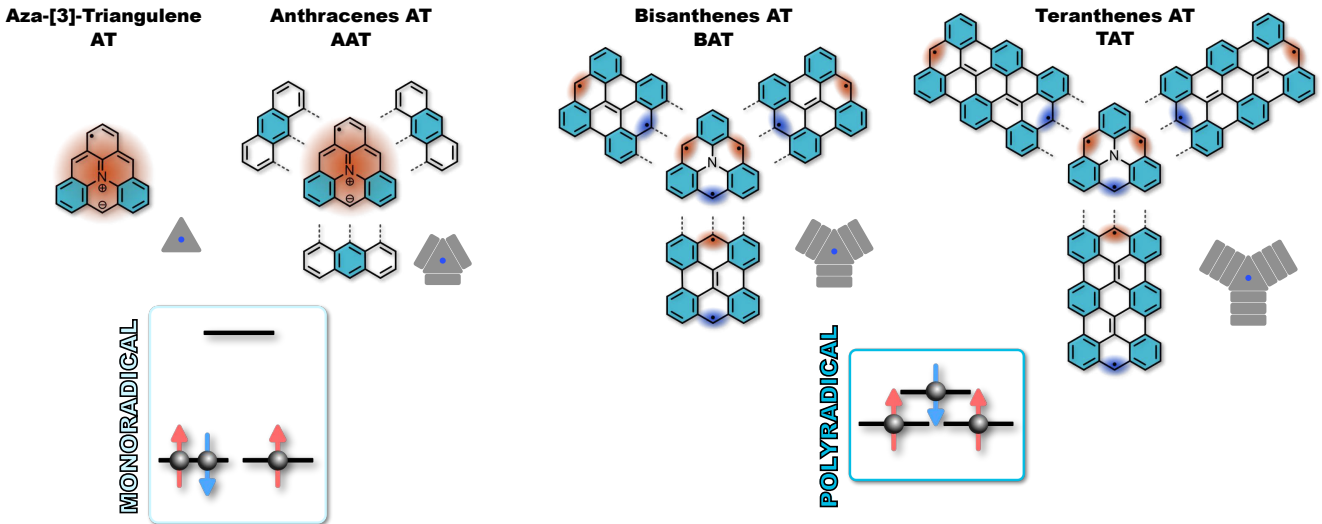


FIG. 1. Construction of the extended aza-triangulene platforms through anthene addition. Progression of open-shell states in aza-[3]-triangulene architectures by incorporation of anthene units with increasing length. The red and blue shadows indicate radical regions. The resulting 7AGNR segments gain open-shell character as their length increases due to a topological transition, forcing the **AT** core to reorganize its electrons in zero-energy modes. The aromatic Clar sextets are colored in light blue. A schematic representation of active energy states and their electron/spin redistribution found in this work is added at the bottom.

with weak antiferromagnetic interactions by covalently extending its zigzag edges with anthracenyl fragments, as illustrated in Fig. 1. The resulting architectures mimic a junction of three 7-carbon-wide armchair graphene nanoribbons (7AGNRs) connected through the **AT** core. For anthenes with length $n > 2$ of anthracene units, 7AGNRs are prone to develop radical states localized at their zigzag termini [37]. These end states originate from the non-trivial topology of the conjugated network [38] and are further stabilized by the increasing number of Clar sextets as the ribbon length grows [39–41] (see Supplementary Fig. S2). Connecting the 7AGNRs through the **AT** core reorganizes the energy balance and electron occupation of the ZESs, thereby favoring a triradical ground state.

We demonstrate this polyyradical progression experimentally by synthesizing and studying the **AAT** ($n = 1$) and **BAT** ($n = 2$) nanographenes, shown in Fig. 1. We combine low-temperature scanning tunneling microscopy (STM) and multi-reference quantum chemical calculations to confirm that these two molecules are located right at the transition to a weakly interacting trimer of spin- $\frac{1}{2}$ states. Remarkably, despite the three radicals residing on the same sublattice, nitrogen doping critically reverses their exchange pattern, leading to weak antiferromagnetic coupling. The presented strategy of merging chemical design with topological transitions demonstrates how nanographene architectures can be modulated to realize frustrated spin systems with potential as molecular quantum registers.

RESULTS

Synthesis of AT-anthrene platforms

The synthesis of **AAT** and **BAT** was achieved via the on-surface reaction of the **AT** derivatives **1** and **2** shown in Fig. 2a. The synthetic strategy followed to obtain these precursors is inspired in the preparation of aza-[5]-triangulene [31]. The synthesis involved a sequence of solution-phase reactions, starting with the treatment of tribenzaldehyde **3** with an excess of organolithium reagents **4** or **5**. Then, BF_3 -promoted, threefold intramolecular Friedel–Crafts cyclization, led to the formation of the **AT** derivatives **1** or **2**, respectively.

Precursors **1** and **2** were deposited on an atomically clean $\text{Au}(111)$ surface held at room temperature by sublimation from a silicon wafer (see Methods in SI). Subsequent annealing at 330°C induced substrate-catalyzed dehydrogenation and cyclodehydrogenation reactions [8], yielding the targeted aza-[3]-triangulene derivatives shown in Fig. 2b. The formation of **AAT** and **BAT** was confirmed by bond-resolved (BR) non-contact atomic force microscopy (nc-AFM) [42] and STM using a CO-functionalized tip. The nc-AFM images (Fig. 2c) reveal the honeycomb lattice of the carbon backbone, with the central nitrogen atom appearing darker, consistent with previous reports on aza-[5]triangulene [31, 32].

Bond-resolved current images in Fig. 2d display enhanced signal surrounding the molecular zigzag edges of both **AAT** and **BAT** architectures. This local enhancement of the tunneling current indicates an increase of the density of states near the Fermi energy at the zigzag termini. As shown below, this feature originates from the

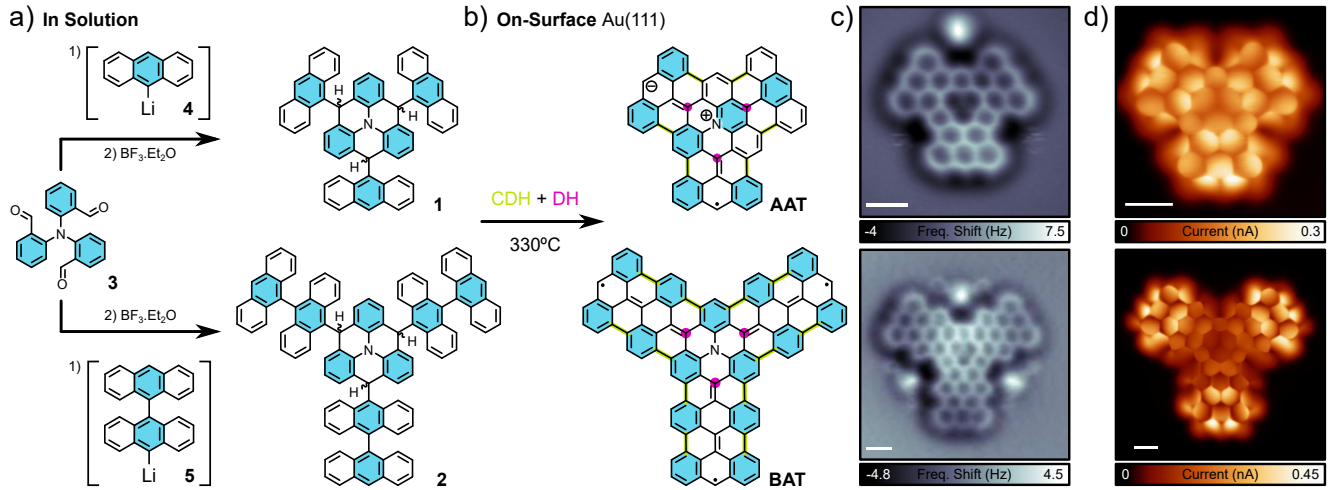


FIG. 2. **Synthesis route of extended AT platforms.** a) Chemical reactions performed in solution to yield the targeted precursors **1** (top) and **2** (bottom). b) Reactions on-surface of cyclodehydrogenation (CDH) and dehydrogenation (DH) leading to the desired planar nanostructures. c) nc-AFM and d) STM images of extended aza platforms **AAT** (top) and **BAT** (bottom) performed with a CO-functionalized tip at constant height with $V = 0\text{ mV}$ and 2 mV , respectively (scalebars 4 Å). The additional bright features in the bay regions of the molecules visible in the nc-AFM images are CO molecules adsorbed next to the nanographenes.

intricate spin structure of the poly-anthracene-extended aza-triangularene core.

Detection of π -magnetic ground state

To unravel the magnetic properties of these nanographenes, we performed low-bias tunneling spectroscopy at the zigzag edges at the termini of both **AAT** and **BAT** molecules. The differential conductance (dI/dV) spectra in Figs. 3a-3d show narrow zero-bias peaks in both molecules, which can be found with a similar line-shape in each of the three zigzag edges (Supplementary Fig. S5). We assign these resonances to Kondo screening of unpaired π -electrons by the conduction electrons in the substrate [22, 26, 46-50].

To resolve the origin of the Kondo state, we measured the evolution of the Kondo resonances under an applied magnetic field. Both molecules exhibit a similar intrinsic linewidth at the lowest temperature of these experiments (Fig. 3c-d), corresponding to Kondo temperatures of approximately $T_K \sim 3\text{ K}$ [44] (see also Supplementary Fig. S5 and Fig. S6). In both cases, applying a magnetic field up to 3 T did not produce a resolvable peak splitting, but only a broadening of the resonance (Figs. 3c-d). This absence of splitting under fields of the order of $\sim 0.5 T_K$ is characteristic of Kondo-screened spin- $\frac{1}{2}$ ground states [46, 51], and rules out an underscreened Kondo effect, typically observed in nanographenes with higher spin [13, 30, 31, 47, 49].

As shown in the constant-height (CH) current maps in Fig. 2d and Fig. 3e-f, the Kondo density of states is delocalized across the entire graphene platform, with enhanced intensity along the zigzag edges. This extended spatial distribution contrasts with the usual localization of $S = \frac{1}{2}$ Kondo resonances at a single radical center,

suggesting the involvement of multiple spin-polarized orbitals. Simulations of Kondo amplitude maps performed within the multi-orbital Kondo theoretical framework of Ref. [45], also shown in Fig. 3e-f, closely reproduce the experimental data. These results confirm that a multi-reference description is essential to capture the spin distribution in the ground state accurately (see Supplementary Fig. S13 and Fig. S14 for the identification of the relevant Kondo orbitals for each species).

The low-energy spectrum of **AAT** exhibits additional features consisting of two bias-symmetric dI/dV steps at $\sim \pm 100\text{ mV}$, which are absent in **BAT** (see Fig. 3a and its numerical derivative). We attribute these steps to inelastic spin excitations induced by tunneling electrons [46]. Given the expected multiradical character of this molecule and considering spin conservation, we assign them to a spin excitation from an $S = \frac{1}{2}$ ground state to an $S = \frac{3}{2}$ excited state. Similar to the Kondo resonance, the inelastic spin signal is delocalized across the entire molecular backbone in the maps shown in Supplementary Fig. S8, with enhanced intensity at the zigzag edges. This spatial distribution is well-reproduced by the set of natural transition orbitals displayed in Supplementary Fig. S8. In contrast, the larger nanographene **BAT** shows no resolvable spin inelastic features, even in spectra acquired at the lowest temperatures.

Transition from single radical to frustrated spin triradical

To decipher the spin configuration in these nanographenes and the origin of inelastic spin excitations, we performed multi-reference quantum chemistry simulations within the Complete Active Space (CAS) frame-

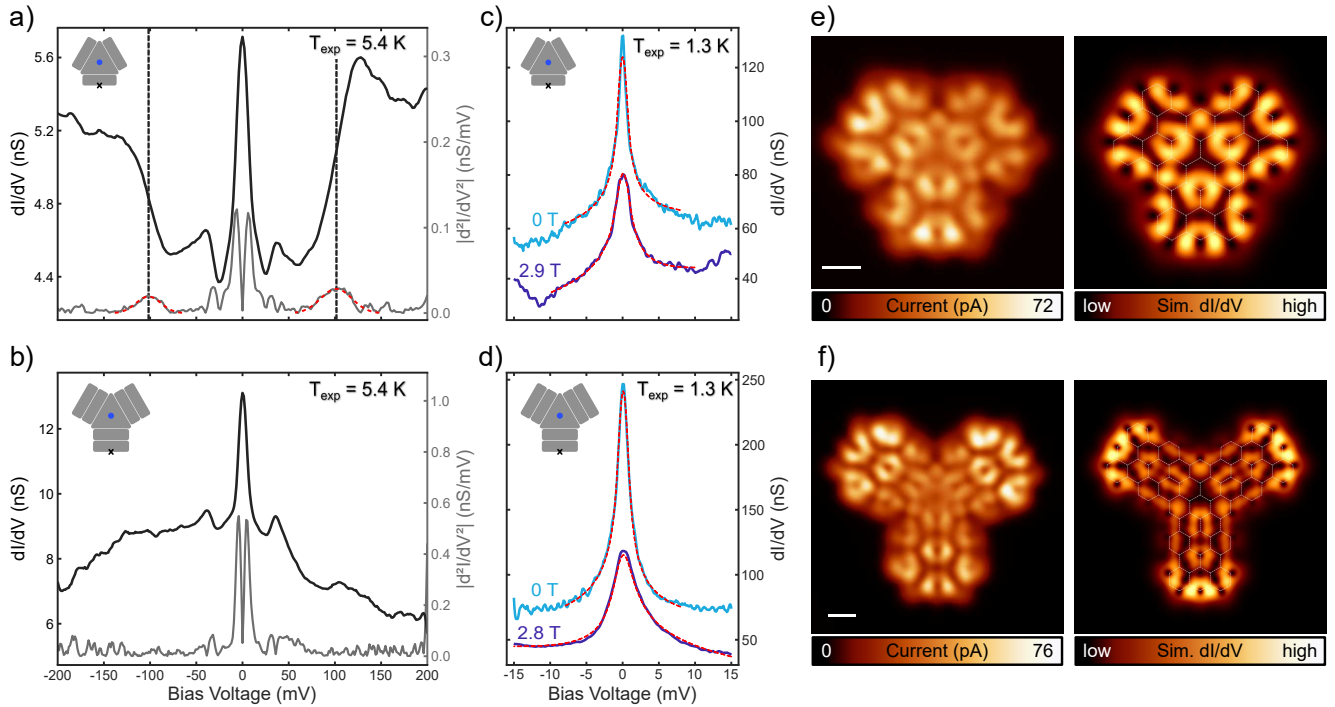


FIG. 3. **Detection of π -magnetism.** Low-energy dI/dV spectra measured over a zigzag edge of a) **AAT** and b) **BAT** with a CO-functionalized tip at 5.4 K. Spectra over all three edges are qualitatively equivalent and featureless on the bare Au (see Fig. S5). Grey plots are the absolute value of the numerically calculated derivative of dI/dV ; dashed lines in a) are Gaussian fits to the inelastic spin excitation signal. Steps at ± 35 mV correspond to external vibrations of the CO molecule at the tip. c,d) High-resolution dI/dV plots of the Kondo resonances at 1.3 K of **AAT** and **BAT**, respectively, with (purple) and without (blue) 2.8 T magnetic field applied. The red-dashed lines are Hurwitz-Fano fits [43, 44] providing intrinsic Kondo linewidths $\Gamma_K = (0.61 \pm 0.03)$ mV and $\Gamma_K = (0.79 \pm 0.03)$ mV, for the zero field case, which corresponds to $T_K = (2.49 \pm 0.05)$ K and $T_K = (2.84 \pm 0.07)$ K for **AAT** and **BAT**, respectively. e,f) Constant-height current Kondo maps of **AAT** and **BAT**, respectively (with a CO-functionalized tip, $V = 2$ mV, scalebars 4 Å, see also Fig. S7), compared with simulated dI/dV maps from the molecular Kondo orbitals (see Methods and [45])

work [27, 29, 52]. We employed the complete active space self-consistent field (CASSCF) method with the N-electron valence state second-order perturbation theory (NEVPT2) correction included for capturing dynamic correlation effects outside the active space [53]. This approach enables a quantitative analysis of the spin states in the aza-nanographene platforms and their excitations.

The simulations shown in Fig. 4 confirm that the global ground state of **AAT** consists of a pair of near-degenerate doublet states, a hallmark of a frustrated spin trimer [54]. This incipient spin frustration arises from the partial occupation of two quasi-degenerate natural orbitals (NO1 and NO2), predominantly localized at the zigzag termini, and a third low-lying orbital (NO3) delocalized over the central region of **AAT**.

The multi-reference simulations also reproduce a low-energy spin-flip transition into a higher-spin quartet, characterized by the single occupancy of each of the three active natural orbitals and, hence, a pronounced triradical character. The computed doublet-quartet excitation involves a much smaller energy scale than the NO3 alignment (exceeding 1 eV in **AAT**), closely matching

the inelastic conductance step observed at approximately ± 100 meV in the STS spectra of **AAT** (Fig. 3a). The detection of this spin excitation with a large cross-section in STS experiments is consistent with the finite polyradical character already present in the ground state through partial occupation of NO3.

Extending the anthene moieties with an additional anthracene in **BAT** clearly enhances its multiconfigurational character by bringing all three natural orbitals close to single occupancy (Fig. 4c). Within this framework, the ground state of **BAT** emerges as a nearly degenerate doublet-quartet manifold (Fig. 4b), reflecting the system's proximity to a regime of effectively three non-interacting spins. The nearly negligible exchange interaction agrees with the absence of inelastic spin excitations in the experimental spectrum of **BAT** (Fig. 3a-b), in contrast to **AAT**. The three quasi-independent $S = \frac{1}{2}$ spins localize at the zigzag edges, as seen in the current maps of Fig. 2d, where each site exhibits its own spin- $\frac{1}{2}$ Kondo resonance (Supplementary Fig. S5).

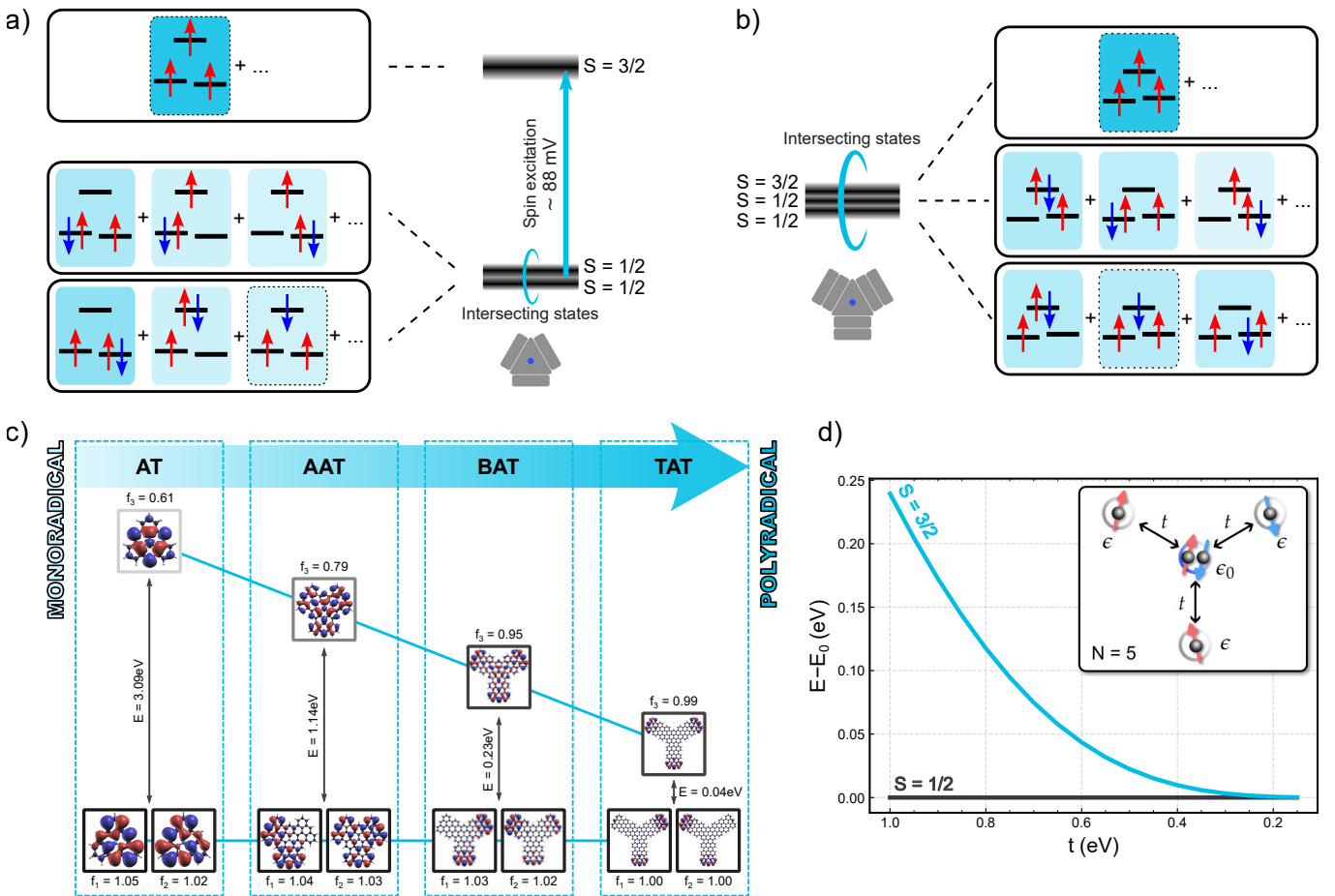


FIG. 4. Spin states and transition from mono to polyradical. Many-body states diagram obtained from multi-reference calculations for a) AAT and b) BAT. It shows the most important spin multiplets of the three lowest energy states. The triradial spin multiplets appear highlighted by dashed lines. c) Scheme of the energy reduction and occupancy increase of the NO₃ as the size of the aza-nanographene increases, extracted from CASSCF(9,11). d) Energy difference between two degenerate doublet states and the excited quartet state as a function of the hopping parameter t , obtained from the Hubbard toy model depicted as an inset (see also Supplementary Fig. 16) for parameters $\varepsilon = 0$, $\varepsilon_0 = -3$ eV, and $U = 2.5$ eV for each of the four orbitals.

DISCUSSION

Our results reveal a gradual evolution from the single-radical character of the **AT** moiety [30, 36], through the frustrated spin trimer observed in **AAT**, to the triradical character of **BAT** as longer anthene units are incorporated. As illustrated in Fig. 4c, this transition is driven by the progressive accumulation of the three most active natural orbitals (NO1–NO3) within a narrow energy window as the molecular size increases, and by the resulting electron reorganization among them. In particular, the lowering of the NO3 energy transforms this orbital from the a_1 -like many-body state centered on the nitrogen atom in **AT** [36] into one localized at the zigzag edges in **TAT**, strongly mixed with NO1 and NO2, thus enabling the delocalization of three unpaired electrons across the termini.

This electronic reconfiguration is reminiscent of the

topological transition in 7AGNRs, where radical end states emerge at the zigzag termini once a topological phase becomes stabilized beyond a critical length [37, 38, 40, 55]. The AT-derived structures can be viewed as three 7AGNR segments connected through the AT core, which hosts a central junction state [56] that becomes doubly occupied by the extra electron donated by nitrogen. The remaining three radicals correspond to 7AGNR-like end states whose spatial overlap progressively decreases as the ribbon length increases.

Despite lying on the same sublattice, the three radicals in the AT-architectures exhibit an antiferromagnetic exchange interaction vanishing with their size. Such spin coupling can be rationalized by modeling the spin trimers with a four-site Hubbard Hamiltonian with five electrons (Fig. 4d). In the ground state, the model consistently yields an antiferromagnetic exchange pattern vanishing

with their coupling, in contrast to an expected Hund alignment [57]. The origin of this is the double occupation of the central site, representing the aza core. Modeling instead a pristine carbon system (Supplementary Fig. S16) produces a complete reversal to ferromagnetic correlations between the terminal spins. While Lieb's theorem is strictly applicable only to half-filled lattices, it is notable that substitution of the central atom with nitrogen reverses the exchange pattern between terminal spins, stabilizing antiferromagnetic correlations.

These results establish **BAT** as a prototypical molecular triradical with topologically protected edge states and very weak exchange interactions, providing an ideal platform to explore correlated spin phenomena at the nanoscale. This spin trimer constitutes a molecular analog of the recently realized three-qubit system based on magnetic adatoms [58]. Benefiting from their weak exchange interaction, the spins of **BAT** can be selectively aligned by external or local magnetic fields and coherently addressed with microwaves, making **BAT** a promising platform for coherent spin manipulation.

CONCLUSION

In summary, we present a molecular design strategy to reconfigure the number of radicals in an open-shell aza-triangulene nanographene by covalently incorporating anthene segments at its zigzag edges. This approach transforms a single-radical doublet into a frustrated spin triradical. The activation of additional radicals arises from the progressive stabilization of a topological phase within the attached anthene segments as their length increases, analogous to the behavior of short 7AGNRs, as revealed by multi-reference quantum calculations. Importantly, we demonstrate that nitrogen substitution in the aza-triangulene core reverses the exchange pattern, offering new chemical routes to control magnetic interactions at the molecular scale. By uniting chemical synthesis with the concepts of spin frustration and topological protection, our work establishes a general design principle for molecular platforms hosting symmetry-protected, weakly coupled spins. Such architectures provide a chemically programmable platform for quantum registers, paving the way toward the coherent manipulation of entangled spin states in graphene-based nanostructures.

The authors acknowledge financial support from grants PID2022-140845OBC61, PID2022-140845OBC62, PID2022-139776NB-C65, PID2023-146694NB-I00, and CEX2020-001038-M funded by MICIU/AEI/10.13039/501100011033 and the European Regional Development Fund (ERDF, A way of making Europe), from the FET-Open project SPRING (863098), the HE project HORIZON-EUROHPC-JU-2021-COE-01 01-101093374-MaX, the ERC Synergy Grant MoldAM (no. 951519), and the ERC-AdG

CONSPIRA (101097693) funded by the European Union, from the European Union NextGenerationEU / PRTR-C17.I1 as well as by the IKUR Strategy of the Department of Education of the Basque Government, and from the Xunta de Galicia (Centro de Investigacion do Sistema Universitario de Galicia, 2023–2027, ED431G 2023/03). F.R.-L., and F.S. acknowledge funding by MICIU/AEI and FSE+ through scholarship No. FPU20/03305, and through the Ramón y Cajal Fellowship RYC2021-034304-I, respectively. R.O. acknowledge financial suport within the scope of the project CICECO-Aveiro Institute of Materials, UIDB/50011/ 2020 (DOI 10.54499/UIDB/50011/2020), UIDP/50011/ 2020 (DOI 10.54499/UIDP/50011/2020), and LA/P/0006/ 2020 (DOI 10.54499/LA/P/0006/2020), financed by national funds through the FCT/MCTES (PIDDAC). P.J., M.K., and D.S. acknowledge the support of the Czech Science Foundation (GACR) project No.23-05486S and the CzechNanoLab Research Infrastructure supported by MEYSCR (LM2018110).

* These authors contributed equally to this work.

† diego.pena@usc.es

‡ ji.pascual@nanogune.eu

- [1] O. V. Yazyev, Emergence of magnetism in graphene materials and nanostructures, *Reports on Progress in Physics* **73**, 056501 (2010).
- [2] D. G. de Oteyza and T. Frederiksen, Carbon-based nanostructures as a versatile platform for tunable π -magnetism, *Journal of Physics: Condensed Matter* **34**, 443001 (2022).
- [3] Y. Yao, F. Ye, X.-L. Qi, S.-C. Zhang, and Z. Fang, Spin-orbit gap of graphene: First-principles calculations, *Physical Review B* **75**, 041401 (2007).
- [4] O. V. Yazyev and M. I. Katsnelson, Magnetic Correlations at Graphene Edges: Basis for Novel Spintronics Devices, *Physical Review Letters* **100**, 047209 (2008).
- [5] O. V. Yazyev, Hyperfine Interactions in Graphene and Related Carbon Nanostructures, *Nano Letters* **8**, 1011 (2008).
- [6] W. L. Wang, O. V. Yazyev, S. Meng, and E. Kaxiras, Topological Frustration in Graphene Nanoflakes: Magnetic Order and Spin Logic Devices, *Physical Review Letters* **102**, 157201 (2009).
- [7] E. Clair and D. G. Stewart, Aromatic Hydrocarbons. LXV. Triangulene Derivatives¹, *Journal of the American Chemical Society* **75**, 2667 (1953).
- [8] S. Clair and D. G. de Oteyza, Controlling a Chemical Coupling Reaction on a Surface: Tools and Strategies for On-Surface Synthesis, *Chemical Reviews* **119**, 4717 (2019).
- [9] N. Pavliček, A. Mistry, Z. Majzik, N. Moll, G. Meyer, D. J. Fox, and L. Gross, Synthesis and characterization of triangulene, *Nature Nanotechnology* **12**, 308 (2017).
- [10] S. Mishra, D. Beyer, K. Eimre, J. Liu, R. Berger, O. Gröning, C. A. Pignedoli, K. Müllen, R. Fasel, X. Feng, and P. Ruffieux, Synthesis and Characterization of π -Extended Triangulene, *Journal of the American*

Chemical Society **141**, 10621 (2019).

[11] J. Su, M. Telychko, P. Hu, G. Macam, P. Mutombo, H. Zhang, Y. Bao, F. Cheng, Z.-Q. Huang, Z. Qiu, S. J. R. Tan, H. Lin, P. Jelínek, F.-C. Chuang, J. Wu, and J. Lu, Atomically precise bottom-up synthesis of π -extended [5]triangulene, *Science Advances* **5**, eaav7717 (2019).

[12] S. Mishra, K. Xu, K. Eimre, H. Komber, J. Ma, C. A. Pignedoli, R. Fasel, X. Feng, and P. Ruffieux, Synthesis and characterization of [7]triangulene, *Nanoscale* **13**, 1624 (2021).

[13] E. Turco, A. Bernhardt, N. Krane, L. Valenta, R. Fasel, M. Jurićek, and P. Ruffieux, Observation of the Magnetic Ground State of the Two Smallest Triangular Nanographenes, *JACS Au* **3**, 1358 (2023).

[14] S. Mishra, D. Beyer, K. Eimre, R. Ortiz, J. Fernández-Rossier, R. Berger, O. Gröning, C. A. Pignedoli, R. Fasel, X. Feng, and P. Ruffieux, Collective All-Carbon Magnetism in Triangulene Dimers, *Angewandte Chemie International Edition* **59**, 12041 (2020).

[15] S. Mishra, G. Catarina, F. Wu, R. Ortiz, D. Jacob, K. Eimre, J. Ma, C. A. Pignedoli, X. Feng, P. Ruffieux, J. Fernández-Rossier, and R. Fasel, Observation of fractional edge excitations in nanographene spin chains, *Nature* **598**, 287 (2021).

[16] J. Hieulle, S. Castro, N. Friedrich, A. Vegliante, F. R. Lara, S. Sanz, D. Rey, M. Corso, T. Frederiksen, J. I. Pascual, and D. Peña, On-Surface Synthesis and Collective Spin Excitations of a Triangulene-Based Nanostar, *Angewandte Chemie International Edition* **60**, 25224 (2021).

[17] S. Cheng, Z. Xue, C. Li, Y. Liu, L. Xiang, Y. Ke, K. Yan, S. Wang, and P. Yu, On-surface synthesis of triangulene trimers via dehydration reaction, *Nature Communications* **13**, 1705 (2022).

[18] N. Krane, E. Turco, A. Bernhardt, D. Jacob, G. Gaudus, D. Passerone, M. Luisier, M. Jurićek, R. Fasel, J. Fernández-Rossier, and P. Ruffieux, Exchange Interactions and Intermolecular Hybridization in a Spin-1/2 Nanographene Dimer, *Nano Letters* **23**, 9353 (2023).

[19] Z. Yuan, X.-Y. Zhang, Y. Jiang, X. Qian, Y. Wang, Y. Liu, L. Liu, X. Liu, D. Guan, Y. Li, H. Zheng, C. Liu, J. Jia, M. Qin, P.-N. Liu, D.-Y. Li, and S. Wang, Fractional Spinon Quasiparticles in Open-Shell Triangulene Spin-1/2 Chains, *Journal of the American Chemical Society* **147**, 5004 (2025).

[20] X. Su, Z. Ding, Y. Hong, N. Ke, K. Yan, C. Li, Y.-F. Jiang, and P. Yu, Fabrication of spin-1/2 Heisenberg antiferromagnetic chains via combined on-surface synthesis and reduction for spinon detection, *Nature Synthesis* **4**, 694 (2025).

[21] C. Zhao, L. Yang, J. C. G. Henriques, M. Ferri-Cortés, G. Catarina, C. A. Pignedoli, J. Ma, X. Feng, P. Ruffieux, J. Fernández-Rossier, and R. Fasel, Spin excitations in nanographene-based antiferromagnetic spin-1/2 Heisenberg chains, *Nature Materials* **24**, 722 (2025).

[22] A. Vegliante, M. Vilas-Varela, R. Ortiz, F. Romero Lara, M. Kumar, L. Gómez-Rodrigo, S. Trivini, F. Schulz, D. Soler-Polo, H. Ahmoum, E. Artacho, T. Frederiksen, P. Jelínek, J. I. Pascual, and D. Peña, On-Surface Synthesis of a Ferromagnetic Molecular Spin Trimer, *Journal of the American Chemical Society* **147**, 19530 (2025).

[23] E. Turco, L. Tejerina, G. Catarina, A. Ortega-Guerrero, N. Krane, L. Gross, M. Jurićek, and S. Mishra, Multiconfigurational Ground State of a Diradicaloid Char-acterized at the Atomic Scale, *Journal of the American Chemical Society* **10.1021/jacs.5c13039** (2025).

[24] E. H. Lieb, Two theorems on the Hubbard model, *Physical Review Letters* **62**, 1201 (1989).

[25] J. Fernández-Rossier and J. J. Palacios, Magnetism in Graphene Nanoislands, *Physical Review Letters* **99**, 177204 (2007).

[26] S. Mishra, D. Beyer, K. Eimre, S. Kezilebieke, R. Berger, O. Gröning, C. A. Pignedoli, K. Müllen, P. Liljeroth, P. Ruffieux, X. Feng, and R. Fasel, Topological frustration induces unconventional magnetism in a nanographene, *Nature Nanotechnology* **15**, 22 (2020).

[27] S. Song, A. Pinar Solé, A. Matéj, G. Li, O. Stetsovych, D. Soler, H. Yang, M. Telychko, J. Li, M. Kumar, Q. Chen, S. Edalatmanesh, J. Brabec, L. Veis, J. Wu, P. Jelinek, and J. Lu, Highly entangled polyyradical nanographene with coexisting strong correlation and topological frustration, *Nature Chemistry* **16**, 938 (2024).

[28] C. Zhao, G. Catarina, J.-J. Zhang, J. C. G. Henriques, L. Yang, J. Ma, X. Feng, O. Gröning, P. Ruffieux, J. Fernández-Rossier, and R. Fasel, Tunable topological phases in nanographene-based spin-1/2 alternating-exchange Heisenberg chains, *Nature Nanotechnology* **19**, 1789 (2024).

[29] E. Li, M. Kumar, X. Peng, T. Shen, D. Soler-Polo, Y. Wang, Y. Teng, H. Zhang, S. Song, J. Wu, P. Jelinek, and J. Lu, *Designer polyyradical nanographenes with strong spin entanglement and perturbation resilience via Clar's goblet extension* (2025), arXiv:2506.05181 [cond-mat].

[30] T. Wang, A. Berdonces-Layunta, N. Friedrich, M. Vilas-Varela, J. P. Calupitan, J. I. Pascual, D. Peña, D. Casanova, M. Corso, and D. G. de Oteyza, Aza-Triangulene: On-Surface Synthesis and Electronic and Magnetic Properties, *Journal of the American Chemical Society* **144**, 4522 (2022).

[31] M. Vilas-Varela, F. Romero-Lara, A. Vegliante, J. P. Calupitan, A. Martínez, L. Meyer, U. Uriarte-Amiano, N. Friedrich, D. Wang, F. Schulz, N. E. Koval, M. E. Sandoval-Salinas, D. Casanova, M. Corso, E. Artacho, D. Peña, and J. I. Pascual, On-Surface Synthesis and Characterization of a High-Spin Aza-[5]-Triangulene, *Angewandte Chemie International Edition* **62**, e202307884 (2023).

[32] J. Lawrence, Y. He, H. Wei, J. Su, S. Song, A. Wania Rodrigues, D. Miravet, P. Hawrylak, J. Zhao, J. Wu, and J. Lu, Topological design and synthesis of high-spin aza-triangulenes without jahn-teller distortions, *ACS Nano* **17**, 20237 (2023).

[33] J. P. Calupitan, A. Berdonces-Layunta, F. Aguilar-Galindo, M. Vilas-Varela, D. Peña, D. Casanova, M. Corso, D. G. de Oteyza, and T. Wang, Emergence of π -Magnetism in Fused Aza-Triangulenes: Symmetry and Charge Transfer Effects, *Nano Letters* **23**, 9832 (2023).

[34] D. Li, O. J. Silveira, T. Matsuda, H. Hayashi, H. Maeda, A. S. Foster, and S. Kawai, On-Surface Synthesis of Tri-aza[5]triangulene through Cyclodehydrogenation and its Magnetism, *Angewandte Chemie International Edition* **63**, e202411893 (2024).

[35] J. Henriques, D. Jacob, A. Molina-Sánchez, G. Catarina, A. T. Costa, and J. Fernández-Rossier, Beyond Spin Models in Orbitally Degenerate Open-Shell Nanographenes, *Nano Letters* **24**, 12928 (2024).

[36] M. E. Sandoval-Salinas, A. Carreras, and D. Casanova, Triangular graphene nanofragments: Open-shell character and doping, *Physical Chemistry Chemical Physics* **21**, 9069 (2019).

[37] S. Wang, L. Talirz, C. A. Pignedoli, X. Feng, K. Müllen, R. Fasel, and P. Ruffieux, Giant edge state splitting at atomically precise graphene zigzag edges, *Nature Communications* **7**, 11507 (2016).

[38] T. Cao, F. Zhao, and S. G. Louie, Topological Phases in Graphene Nanoribbons: Junction States, Spin Centers, and Quantum Spin Chains, *Physical Review Letters* **119**, 076401 (2017).

[39] E. Clar, The Aromatic Sextet, in *Mobile Source Emissions Including Polycyclic Organic Species*, edited by D. Rondia, M. Cooke, and R. K. Haroz (Springer Netherlands, Dordrecht, 1983) pp. 49–58.

[40] M. R. Ajayakumar, J. Ma, and X. Feng, π -Extended peri-Acenes: Recent Progress in Synthesis and Characterization, *European Journal of Organic Chemistry* **2022**, e202101428 (2022).

[41] G. Trinquier and J.-P. Malrieu, Predicting the Open-Shell Character of Polycyclic Hydrocarbons in Terms of Clar Sextets, *The Journal of Physical Chemistry A* **122**, 1088 (2018).

[42] L. Gross, F. Mohn, N. Moll, P. Liljeroth, and G. Meyer, The Chemical Structure of a Molecule Resolved by Atomic Force Microscopy, *Science* **325**, 1110 (2009).

[43] D. Jacob, Temperature evolution of the Kondo peak beyond Fermi liquid theory, *Physical Review B* **108**, L161109 (2023).

[44] E. Turco, M. Aapro, S. C. Ganguli, N. Krane, R. Drost, N. Sobrino, A. Bernhardt, M. Juríćek, R. Fasel, P. Ruffieux, P. Liljeroth, and D. Jacob, Demonstrating Kondo behavior by temperature-dependent scanning tunneling spectroscopy, *Physical Review Research* **6**, L022061 (2024).

[45] A. Calvo-Fernández, M. Kumar, D. Soler-Polo, A. Eiguren, M. Blanco-Rey, and P. Jelínek, Theoretical model for multiorbital Kondo screening in strongly correlated molecules with several unpaired electrons, *Physical Review B* **110**, 165113 (2024).

[46] J. Li, S. Sanz, M. Corso, D. J. Choi, D. Peña, T. Frederiksen, and J. I. Pascual, Single spin localization and manipulation in graphene open-shell nanostructures, *Nature Communications* **10**, 200 (2019).

[47] J. Li, S. Sanz, J. Castro-Esteban, M. Vilas-Varela, N. Friedrich, T. Frederiksen, D. Peña, and J. I. Pas-
cual, Uncovering the Triplet Ground State of Triangular Graphene Nanoflakes Engineered with Atomic Precision on a Metal Surface, *Physical Review Letters* **124**, 177201 (2020).

[48] S. Mishra, D. Beyer, R. Berger, J. Liu, O. Gröning, J. I. Urgel, K. Müllen, P. Ruffieux, X. Feng, and R. Fasel, Topological Defect-Induced Magnetism in a Nanographene, *Journal of the American Chemical Society* **142**, 1147 (2020).

[49] X. Su, C. Li, Q. Du, K. Tao, S. Wang, and P. Yu, Atomically Precise Synthesis and Characterization of Hepta-threne with Triplet Ground State, *Nano Letters* **20**, 6859 (2020).

[50] H. Zhang, J. Lu, Y. Zhang, L. Gao, X.-J. Zhao, Y.-Z. Tan, and J. Cai, Magnetism engineering of nanographene: An enrichment strategy by co-depositing diverse precursors on Au(111), *Chinese Chemical Letters* **34**, 107450 (2023).

[51] J. Kondo, Resistance Minimum in Dilute Magnetic Alloys, *Progress of Theoretical Physics* **32**, 37 (1964).

[52] M. Kumar, D. Soler-Polo, M. Lozano, E. Monino, L. Veis, and P. Jelinek, Multireference Theory of Scanning Tunneling Spectroscopy Beyond One-Electron Molecular Orbitals: Can We Image Molecular Orbitals?, *Journal of the American Chemical Society* **147**, 24993 (2025).

[53] C. Angeli, M. Pastore, and R. Cimiraglia, New perspectives in multireference perturbation theory: The n -electron valence state approach, *Theoretical Chemistry Accounts* **117**, 743 (2007).

[54] J. T. Haraldsen, T. Barnes, and J. L. Musfeldt, Neutron Scattering and Magnetic Observables for $S = 1/2$ Molecular Magnets, *Physical Review B* **71**, 064403 (2005).

[55] J. Lawrence, P. Brandimarte, A. Berdonces-Layunta, M. S. G. Mohammed, A. Grewal, C. C. Leon, D. Sánchez-Portal, and D. G. de Oteyza, Probing the Magnetism of Topological End States in 5-Armchair Graphene Nanoribbons, *ACS Nano* **14**, 4499 (2020).

[56] G. Tamaki, T. Kawakami, and M. Koshino, Topological junction states and their crystalline network in systems with chiral symmetry: Application to graphene nanoribbons, *Physical Review B* **101**, 205311 (2020).

[57] D. Jacob and J. Fernández-Rossier, Theory of intermolecular exchange in coupled spin- $\frac{1}{2}$ nanographenes, *Physical Review B* **106**, 205405 (2022).

[58] Y. Wang, Y. Chen, H. T. Bui, C. Wolf, M. Haze, C. Mier, J. Kim, D.-J. Choi, C. P. Lutz, Y. Bae, S.-h. Phark, and A. J. Heinrich, An atomic-scale multi-qubit platform, *Science* **382**, 87 (2023).

Supplementary Information:
Topological Engineering of a Frustrated Antiferromagnetic Triradical in
Aza-Triangulene Architectures

Francisco Romero-Lara,^{1,*} Manuel Vilas-Varela,^{2,*} Ricardo Ortiz,^{3,4,*} Manish Kumar,⁵ Alessio Vegliante,¹ Lucía Gómez-Rodrigo,² Jan Patrick Calupitan,^{3,6,7} Diego Soler,⁵ Nikas Friedrich,¹ Dongfei Wang,^{1,8} Jon Ortuzar,¹ Stefano Trivini,¹ Fabian Schulz,¹ Thomas Frederiksen,^{3,9} Pavel Jelínek,⁵ Diego Peña,^{2,10,†} and Jose Ignacio Pascual^{1,9,‡}

¹*CIC nanoGUNE-BRTA, 20018 Donostia-San Sebastián, Spain*

²*Centro Singular de Investigación en Química Biolóxica e Materiais Moleculares (CiQUS) and Departamento de Química Orgánica, Universidad de Santiago de Compostela, 15782 Santiago de Compostela, Spain*

³*Donostia International Physics Center (DIPC), 20018 Donostia-San Sebastian, Spain*

⁴*CICECO- Aveiro Institute of Materials, Department of Chemistry, University of Aveiro, 3810-193 Aveiro, Portugal*

⁵*Institute of Physics of the Czech Academy of Sciences, Cukrovarnická 10, Prague 6, CZ 16200, Czech Republic*

⁶*Centro de Física de Materiales (CFM-MPC), Centro Mixto CSIC-UPV/EHU, E-20018 Donostia-San Sebastián, Spain*

⁷*Sorbonne Université, CNRS, Institut Parisien de Chimie Moléculaire (IPCM), F-75005 Paris, France*

⁸*School of Physics; Centre for Quantum Physics, Beijing Institute of Technology, 100081 Beijing, China*

⁹*Ikerbasque, Basque Foundation for Science, 48009 Bilbao, Spain*

¹⁰*Oportunius, Galician Innovation Agency (GAIN), 15702 Santiago de Compostela, Spain*

(Dated: December 12, 2025)

CONTENTS

| | |
|--|----|
| I. Methods | 2 |
| II. In solution synthesis of molecular precursors | 3 |
| III. Supplementary experimental and theoretical results | 5 |
| A. Clar sextets counting | 5 |
| B. Frequently observed fragments | 6 |
| C. Tip-induced removal of extra H-atoms | 7 |
| D. Comparison of STS spectra over each zigzag edge | 8 |
| E. Temperature- and magnetic field-dependent STS of AAT | 9 |
| F. Comparison between I , dI/dV , and CITS Kondo maps for BAT | 9 |
| G. IETS mapping of the spin excitation of AAT | 10 |
| H. Orbital mapping and Dyson orbitals | 11 |
| I. CASCI Calculations | 12 |
| J. Kondo orbitals simulations | 13 |
| K. CASSCF calculations | 15 |
| L. Hubbard toy-model | 16 |
| M. CAS-Hubbard calculations | 17 |
| References | 20 |

* These authors contributed equally to this work.

† diego.pena@usc.es

‡ ji.pascual@nanogune.eu

I. METHODS

Experimental setup

The experiments were conducted in three different scanning tunneling microscope (STM) setups under ultrahigh vacuum conditions. Two are home-built systems hosting a *Createc GmbH* STM/AFM head with a base temperature of 5 K. The third is a commercial Joule-Thompson (JT) STM from *Specs GmbH* with a base temperature of 1.2 K and equipped with superconducting coils to induce an out-of-plane magnetic field up to 3 T.

On-surface synthesis

The Au(111) single crystal (*MaTeck GmbH*) is prepared by successive cycles of Ne^+ or Ar^+ sputtering and annealing (550 °C) for an atomically flat surface. The molecular precursors were deposited by fast sublimation from a homemade flash silicon evaporator at high temperatures. Alternatively, we deposited molecular precursor **1** in a controlled way from a Knudsen cell at 300 °C using a commercial evaporator from *Dodecon GmbH*. We prepared samples, including either precursor individually or both on the same surface. After the deposition, samples are typically annealed to around 330 °C to induce the planarization reactions, as mentioned in the main text.

Imaging and spectroscopic measurements

All STM and nc-AFM images were acquired under the specific conditions described in each figure caption and processed using the WSxM software [1]. Bond-resolved imaging was typically performed using a CO-functionalized tip at close tip-sample distances, within the regime dominated by repulsive Pauli forces, operating in constant-height mode with bias voltages of less than 5 mV.

Scanning tunneling spectroscopy (STS) measurements were conducted in open-feedback mode under various conditions, employing a lock-in amplifier technique. The presented spectra have been smoothed using a Savitzky–Golay filter, with window sizes ranging from 11 to 15 points and polynomial orders ranging from 3 to 5. Kondo resonances were fitted using a Hurwitz–Fano function convoluted with the AC lock-in broadening, allowing extraction of the intrinsic Kondo width, as detailed in Ref. [2]. The temperature dependence of the intrinsic Kondo width can be fitted to extract the Kondo temperature. Ref. [2] introduces an equation to extract the Kondo temperature from a single point, as we did in Fig. 3 in the main text.

DFT and Multireference calculations

The molecular geometries were optimized using density functional theory (DFT) in high-spin state, as implemented in the FHI-AIMS software package [3], employing the PBE0 hybrid functional [4]. In these calculations, the Tkatchenko-Scheffler method was used to account for Van der Waals interactions. Given the open-shell and multi-radical nature of the molecules, the complete active space configuration interaction (CASCI) method was employed to obtain an accurate description of the wave function and electronic energies. One- and two-electron integrals are constructed in the basis of molecular orbitals around the Fermi energy using the PBE functional, which were derived using the quantum chemistry software ORCA [5] using the orbitals from the restricted open-shell Kohn-Sham (ROKS). Natural orbitals are obtained by diagonalizing the one-particle reduced density matrix constructed from the ground state of the ground-state multireference CASCI wavefunction.

Natural Transition Orbitals (NTO): To simulate the dI/dV maps corresponding to IETS spin excitation maps, we have calculated the Natural Transition Orbitals (NTOs) [6], which correspond to the electronic transition density matrix of the single spin flip process from the first and second doublet ground state to the quartet excited states.

Dyson Orbitals: To accurately interpret experimental differential conductance (dI/dV) maps for these molecules exhibiting significant multireference character, we have calculated the Dyson orbitals [7–9]. They represent the overlap between the many-body wavefunctions before and after electron addition or removal, capturing the spatial distribution of the states directly involved in tunneling.

Kondo Orbitals (KO): Kondo orbitals are calculated by diagonalizing the Hamiltonian derived from the multi-channel Anderson model, which considers the many-body multiplet structure of molecules obtained from the CASCI calculation for the neutral ground state and virtual charge states as described in the Ref. [10].

Theoretical dI/dV maps of NTOs, Kondo, and Dyson orbitals were calculated using the Probe Particle Scanning Probe Microscopy (PP-SPM) code [11].

II. IN SOLUTION SYNTHESIS OF MOLECULAR PRECURSORS

Starting materials were purchased reagent grade from TCI and Sigma-Aldrich and used without further purification. Trimethyl 2,2',2"-nitrilotribenzaldehyde (**3**) was synthesized following a reported procedure [12]. Organolithium reagents (**4** and **5**) were prepared by treatment of the corresponding halides with n-butyllithium [13]. All reactions were carried out in oven-dried glassware, which was cooled down under an inert atmosphere of purified Ar using Schlenk techniques. Thin-layer chromatography (TLC) was performed on Silica Gel 60 F-254 plates (Merck). Column chromatography was performed on silica gel (40-60 μ m). NMR spectra were recorded on a Bruker Varian Inova 500 spectrometer.

Synthesis of precursor **1** (AAT)

Over a solution of the lithium derivative **4** (2.30 mmol, 5.00 equiv.) in THF (20 mL), aldehyde **3** (150 mg, 0.46 mmol) was added at 0°C. After the addition, the mixture was allowed to reach room temperature and was stirred for 16 h. Then, MeOH (2 mL) was added, and the solvent was evaporated under reduced pressure. The residue was redissolved in CH_2Cl_2 (25 mL), and $\text{BF}_3\cdot\text{OEt}_2$ (1.00 mL) was added at 0°C. After the addition, the mixture was stirred for 30 min and poured into an aqueous NaOH solution (2 M, 30 mL). After separating phases, the organic extract was dried over anhydrous Na_2SO_4 , filtered, and evaporated under reduced pressure. The residue was purified by column chromatography (SiO_2 ; hexane: CH_2Cl_2 3:2), affording compound **1** (38 mg, 10%) as a yellow solid.

$^1\text{H NMR}$ (500 MHz, CDCl_3) δ : 8.67 – 8.55 (m, 2H), 8.49 (m, 1H), 8.10 (m, 1H), 8.03 – 7.97 (m, 1H), 7.62 (m, 1H), 7.56 – 7.50 (m, 1H), 7.46 – 7.35 (m, 3H), 6.46 – 6.39 (m, 2H), 6.34 – 6.27 (m, 1H) ppm.

$^{13}\text{C NMR-DEPT}$ (125 MHz, CDCl_3) δ : 139.08 (C), 138.79 (C), 133.11 (C), 133.07 (C), 132.85 (C), 132.66 (C), 132.08 (C), 132.05 (C), 131.32 (C), 129.69 (CH), 129.66 (CH), 129.54 (CH), 129.48 (CH), 129.39 (C), 129.30 (C), 128.27 (CH), 128.16 (CH), 128.13 (CH), 128.02 (CH), 127.99 (CH), 127.45 (CH), 127.38 (CH), 126.85 (CH), 126.79 (CH), 125.79 (CH), 125.66 (C), 125.34 (C), 125.19 (C), 125.15 (CH), 125.11 (CH), 124.89 (CH), 124.85 (CH), 123.58 (CH), 123.44 (CH), 123.23 (CH), 123.05 (CH), 39.03 (CH) ppm.

MS (MALDI-TOF) for $\text{C}_{63}\text{H}_{39}\text{N}$; calculated: 809.31, found: 809.28.

Synthesis of precursor **2** (BAT)

Over a solution of the lithium derivative **5** (0.55 mmol, 4.00 equiv) in THF (15 mL), aldehyde **3** (46 mg, 0.14 mmol) was added at 0°C. After the addition, the mixture was allowed to reach room temperature and was stirred for 16 h. Then, water (10 mL) was added, and the solvent was evaporated under reduced pressure. The residue was redissolved in CH_2Cl_2 (20 mL), and $\text{BF}_3\cdot\text{OEt}_2$ (700 μ L) was added at 0°C. After the addition, the mixture was stirred for 30 min and poured into an aqueous NaOH solution (2 M, 50 mL). After separating phases, the organic extract was dried over anhydrous Na_2SO_4 , filtered, and evaporated under reduced pressure. The residue was purified by column chromatography (SiO_2 ; hexane: CH_2Cl_2 3:2), affording compound **2** (39 mg, 21%) as a yellow solid.

$^1\text{H NMR}$ (500 MHz, CDCl_3) δ : 8.93 – 8.79 (m, 2H), 8.70 (m, 1H), 8.22 – 8.10 (m, 2H), 7.71 (m, 1H), 7.62 (m, 1H), 7.50 – 7.39 (m, 3H), 7.25 – 7.18 (m, 4H), 7.18 – 7.07 (m, 3H), 7.03 (m, 1H), 6.84 (m, 1H), 6.76 (m, 1H), 6.68 (m, 1H) ppm.

$^{13}\text{C NMR-DEPT}$ (125 MHz, CDCl_3) δ : 139.65 (C), 134.34 (C), 134.29 (C), 133.69 (C), 133.58 (C), 133.16 (C), 133.12 (C), 132.99 (C), 132.88 (C), 131.96 (C), 131.86 (C), 131.82 (C), 131.81 (C), 131.74 (C), 131.73 (C), 131.69 (C), 131.22 (C), 131.18 (C), 129.23 (C), 129.08 (C), 128.73 (CH), 128.67 (CH), 128.54 (C), 128.43 (CH), 128.30 (CH), 128.26 (CH), 128.18 (CH), 127.42 (CH), 127.36 (CH), 127.16 (CH), 127.06 (CH), 126.99 (CH), 126.18 (C), 126.12 (CH), 126.08 (CH), 125.95 (CH), 125.80 (CH), 125.76 (C), 125.60 (CH), 125.56 (CH), 125.53 (CH), 125.45 (CH), 125.40 (CH), 125.33 (CH), 123.88 (CH), 123.71 (CH), 123.62 (CH), 123.58 (CH), 39.36 (CH) ppm.

MS (MALDI-TOF) for $\text{C}_{105}\text{H}_{63}\text{N}$; calculated: 1337.50, found: 1337.43.

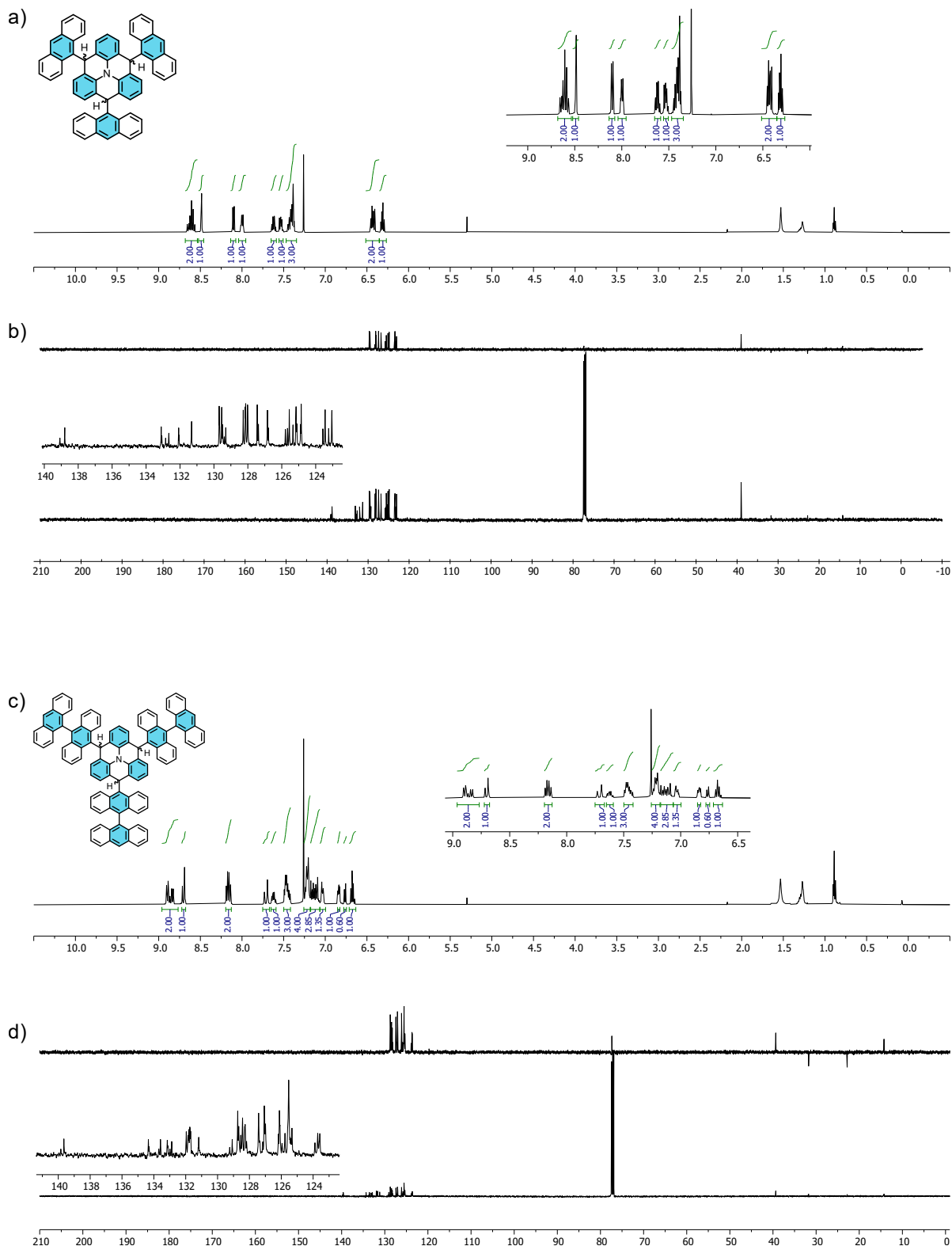


Figure S1. ^1H NMR (500 MHz, CDCl_3) spectrum of compound a) **1** and c) **2**. ^{13}C NMR-DEPT (125 MHz, CDCl_3) spectrum of compound a) **1** and d) **2**.

III. SUPPLEMENTARY EXPERIMENTAL AND THEORETICAL RESULTS

A. Clar sextets counting

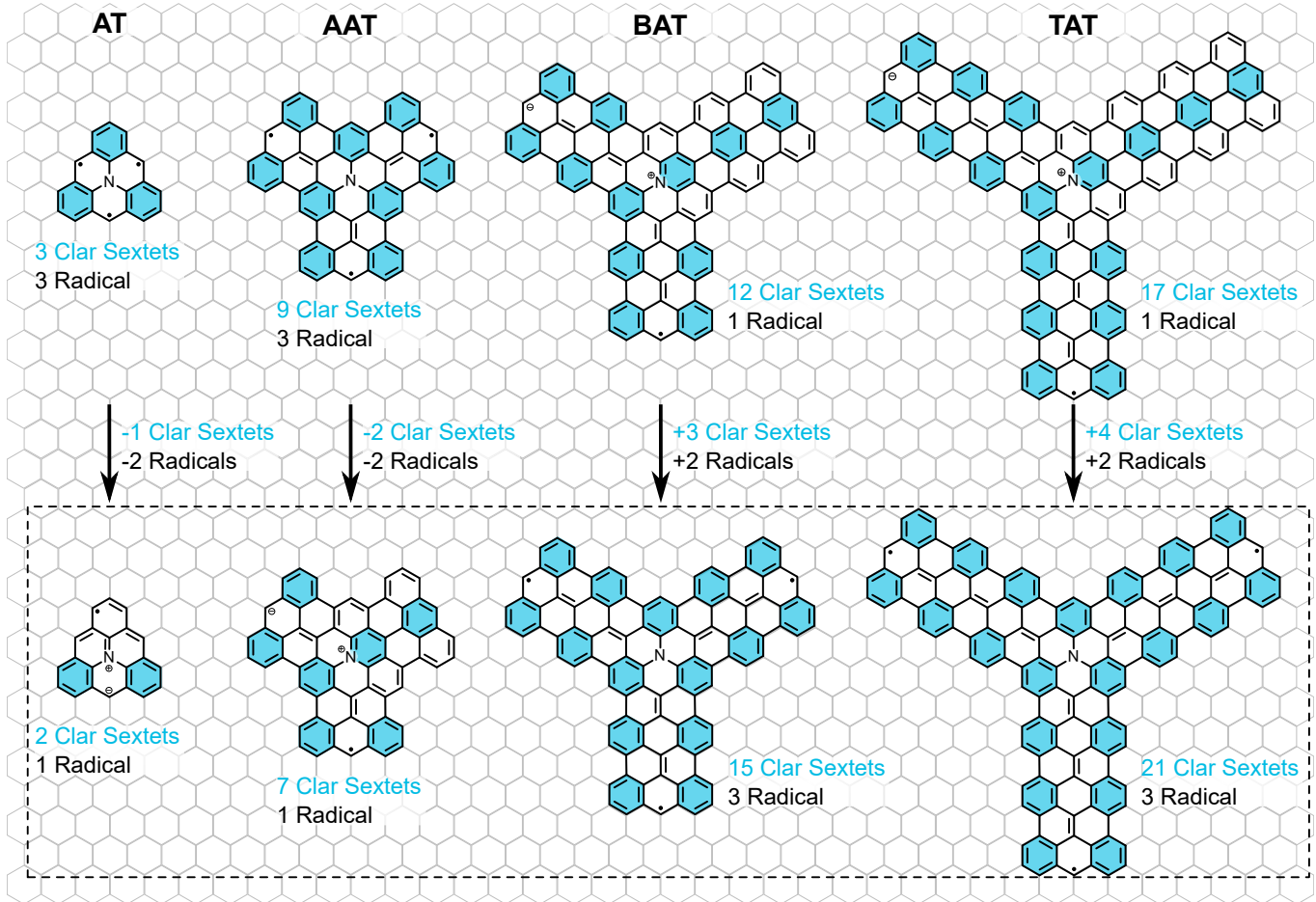


Figure S2. Considering the energetics of Clar sextet formation and π -bond breaking, we predict the transition from monoradical to triradical [14–16]. The dashed rectangle highlights the expected most stable structures.

B. Frequently observed fragments

While our primary focus remains on the intact nanographenes, we frequently encountered twofold symmetric structures (highlighted by the white squares in Fig. S3b and Fig. S3e). We can attribute them to the product of a fragmented precursor. Such precursors occasionally lose one or more anthracene extensions upon deposition on the surface. A proof of this fragmentation can be seen in Fig. S3a. Threefold structures corresponding to the unreacted precursor and smaller elongated structures corresponding to the fragmented anthracenes can be seen. Interestingly, the fragments can host unpaired electrons and readily capture additional hydrogen atoms as seen in Fig. S3c-f.

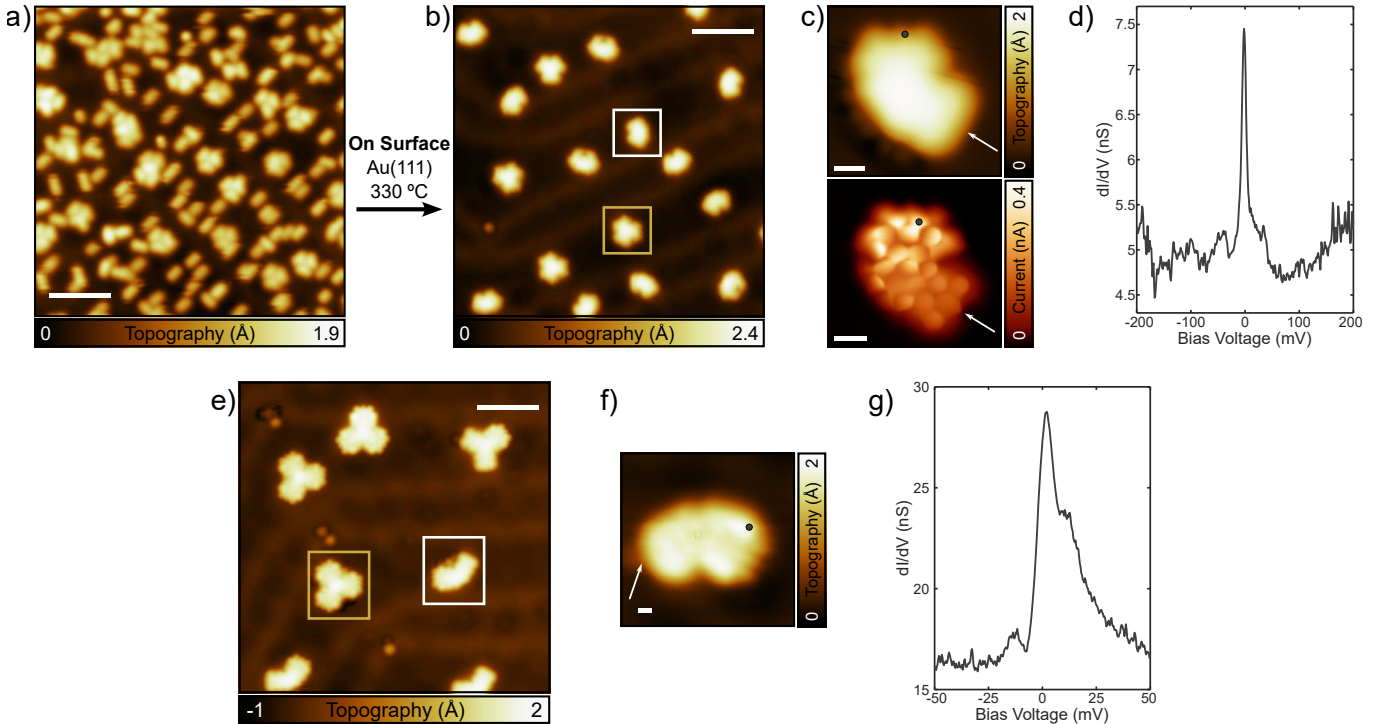


Figure S3. a) Image of the sample showing several unreacted precursors **1** and a large amount of anthracenes, products of the fragmentation upon sublimation. b) and e) Overview image of the sample after the reaction on-surface for **AAT** and **BAT**, respectively. Yellow squares highlight the targeted nanographenes, while white squares highlight the twofold fragments. c) STM (top) and BR-STM (bottom) image of a twofold fragment of **AAT**. White arrows point to extra hydrogen. d) STS spectrum measured over the gray dot in c) showing a Kondo peak at zero bias. f) STM image of a twofold fragment of **BAT**. A white arrow points to an extra hydrogen. d) STS spectrum measured over the gray dot in c) showing a Kondo peak at zero bias. a) and b): scalebars 4 nm, $I=50$ pA, $V=200$ mV; c): scalebars 4 Å, $I=50$ pA, $V=200$ mV (top), $V=5$ mV (bottom); e): scale 4 nm, $I=30$ pA, $V=100$ mV; f): scalebar 4 nm, $I=30$ pA, $V=5$ mV.

C. Tip-induced removal of extra H-atoms

We sometimes encountered additional hydrogen atoms bonded to carbons at the zigzag edges, effectively quenching radical electrons. Both nc-AFM and STM can detect this. Specifically, the extra hydrogen atom yields a brighter contrast in nc-AFM due to the change in hybridization of the carbon from sp^2 to sp^3 , as in Fig. S4c. Conversely, the BR-STM image of the zigzag edge where the radical has been quenched shows a darker contrast, as in Fig. S4b and f. This contrast arises due to the decreased density of states near the Fermi level on this particular edge. These hydrogen atoms can be easily removed through high-energy electron tunneling. Fig. S4e shows a sweep of bias voltage at constant height, revealing a current drop when the extra H is removed.

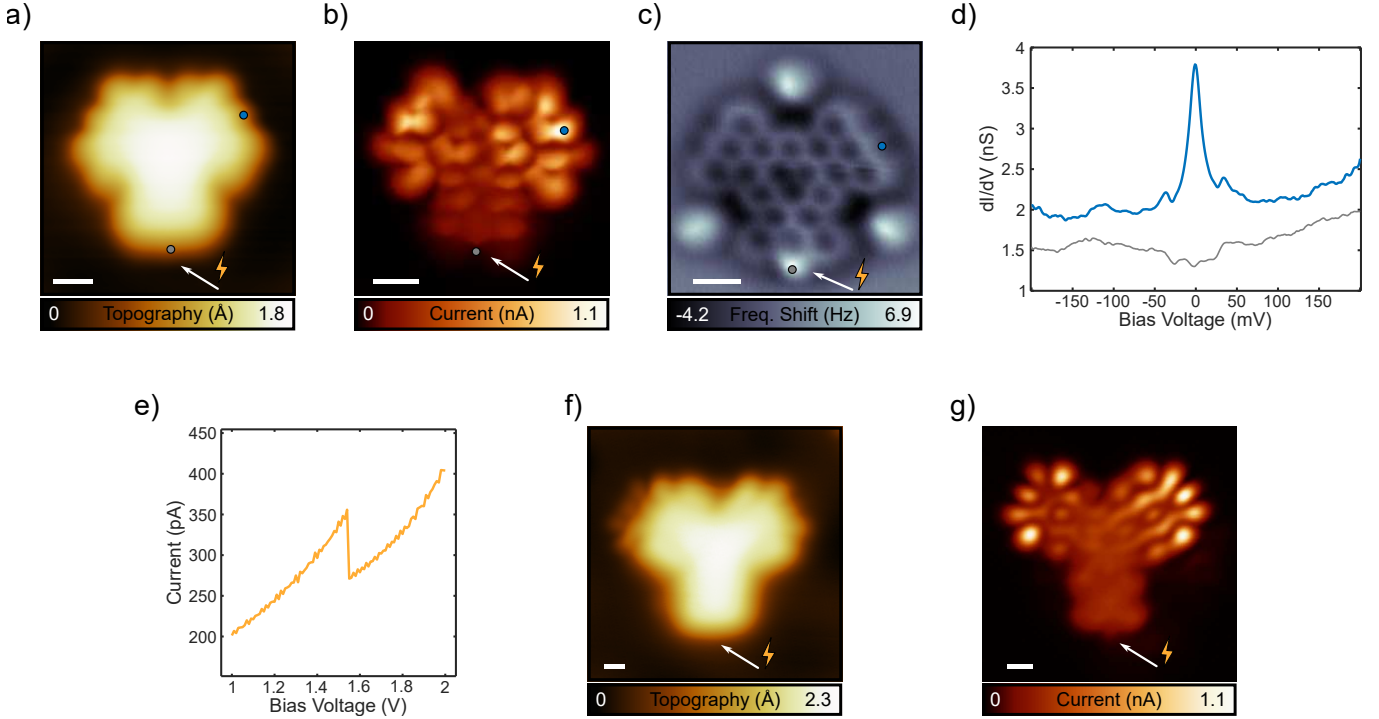


Figure S4. a) and f) STM image of **AAT** and **BAT** respectively with the bottom zigzag edge quenched by an extra hydrogen atom (white arrow). b) and g) BR-STM image of **AAT** and **BAT** with extra H (white arrow). c) nc-AFM image of **AAT** with extra H (white arrow). d) STS spectra measured over a pristine (blue) and quenched (gray) zigzag edge of **AAT** as marked by the colored dots in a), b), and c). e) Typical current vs bias voltage sweep employed to remove extra hydrogens in these structures. a): $I = 50$ pA, $V = 200$ mV; b): $V = 5$ mV; c): $V = 0$ mV; f): $I = 30$ pA, $V = 100$ mV; g): $V = 5$ mV. Scalebars: 4 Å.

D. Comparison of STS spectra over each zigzag edge

Qualitatively equivalent STS spectra are measured independently of the zigzag edge as in Fig. S5a. Fig. S5c shows two spectra measured with the same CO tip yielding similar Kondo lineshapes but with less zero-bias conductance for **AAT**. The inelastic fingerprints of the spin excitation are only present in **AAT**.

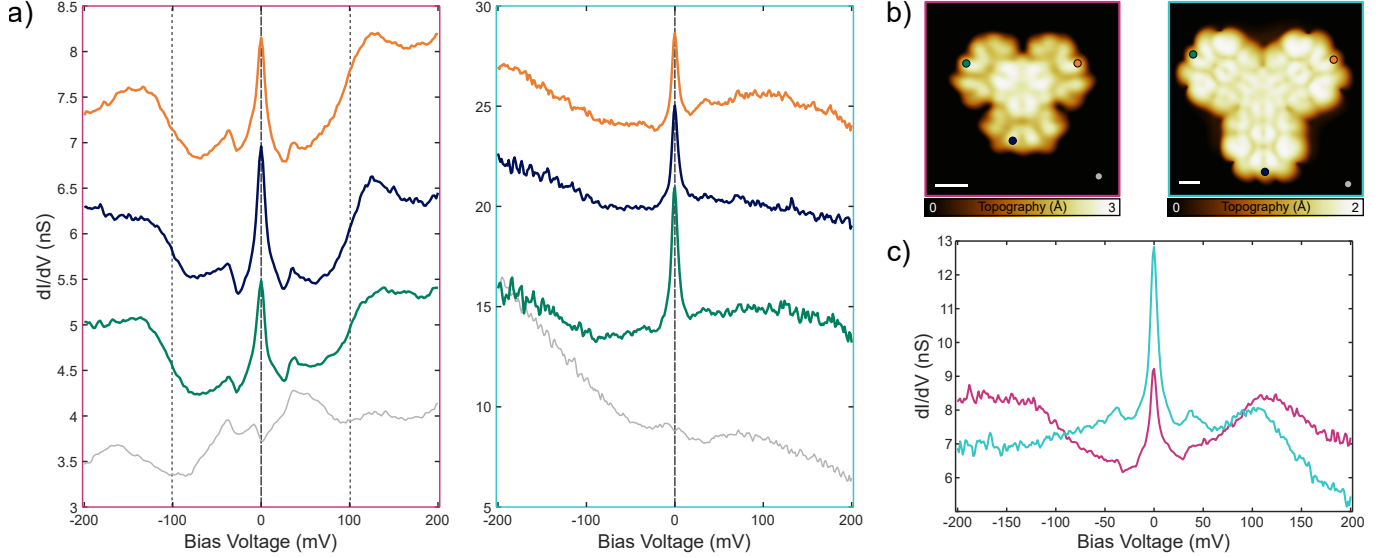


Figure S5. a) STS spectra measured over each zigzag edge and on the bare substrate for **AAT** (left) and **BAT** (right) as indicated by the colored dots in b). Spectra were shifted vertically for clarity, and dashed lines were added as visual guides for Kondo and spin excitation. b) High-resolution CO-STM images of **AAT** (left) and **BAT** (right). c) STS spectra measured with the same tip for **AAT** and **BAT** in one zigzag edge. b) left: $I=50$ pA, $V=5$ mV; right: $I=20$ pA, $V=2$ mV. Scalebar 4 Å.

E. Temperature- and magnetic field-dependent STS of AAT

The Kondo resonance's temperature and magnetic field dependence in **AAT** fits the canonical $S = 1/2$ behaviour.

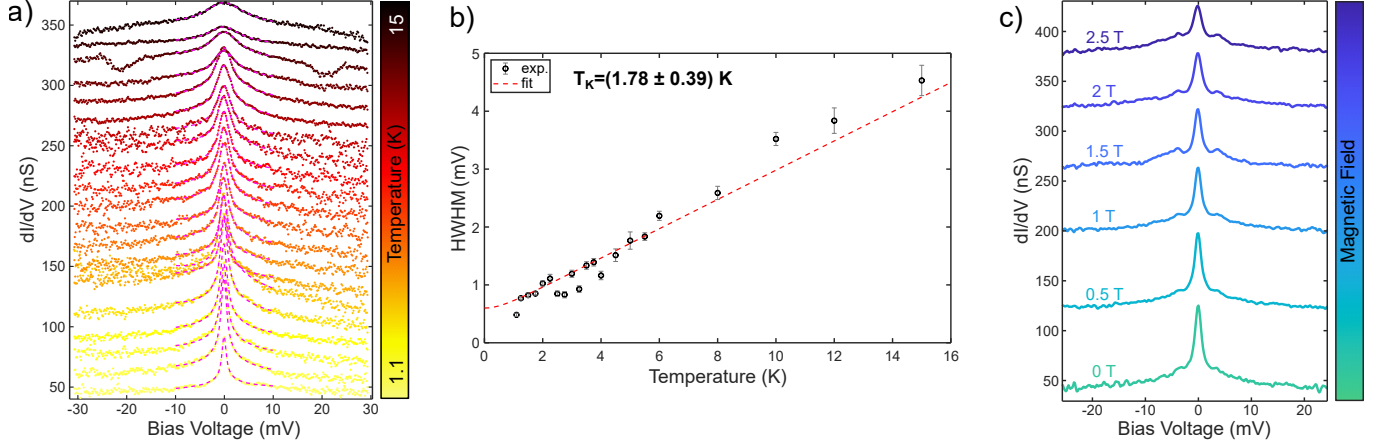


Figure S6. a) Temperature dependence of the Kondo resonance in **AAT**. The pink-dashed lines represent Hurwitz-Fano fits, which include thermal and lock-in broadenings [2]. The spectra are shifted vertically for clarity. b) Intrinsic half-width at half maximum of the Kondo resonance extracted from the fits in a). We extract a Kondo temperature (T_K) of slightly below 2 K by fitting to the expression: $HWHM(T) = 1.542k_B T_K \sqrt{2.732 + 3.732\sqrt{1 + (\pi k_B T / 1.542k_B T_K)^2} + 0.866(\pi k_B T / 1.542k_B T_K)^2}$ [2, 17] (red dashed line). c) Magnetic field dependence of the Kondo resonance in **AAT**. There's no observable splitting for field values below 3 T.

F. Comparison between I , dI/dV , and CITS Kondo maps for BAT

In Fig. 3b of the main manuscript, we experimentally map the Kondo orbitals by acquiring a constant-height CO image of the molecules at a very low bias voltage and tunnel junction resistances of approximately $25 \text{ M}\Omega$. In STM, molecular orbitals are typically visualized through a lock-in amplifier's dI/dV demodulated signal. However, when the DC bias voltage is comparable to the amplitude of the AC signal, both the current and the dI/dV demodulated signal produce the same image, as shown in Fig. S7a and b for the case of **BAT**. Another approach to visualizing molecular orbitals is current imaging tunneling spectroscopy (CITS), which involves measuring a matrix of dI/dV point spectra over the molecule at constant height, always starting from the same tunneling setpoint. This method allows mapping the conductance evolution across the bias range covered by the point spectra, including at 0 bias voltage. In Fig. S7c, we present dI/dV maps at 2 mV and 0 mV for **BAT**, which qualitatively reveal the same molecular distribution as in the previous maps. Current Kondo maps, as shown in Fig. S7a, simplify the process by avoiding lock-in demodulation, resulting in faster acquisition and better image quality.

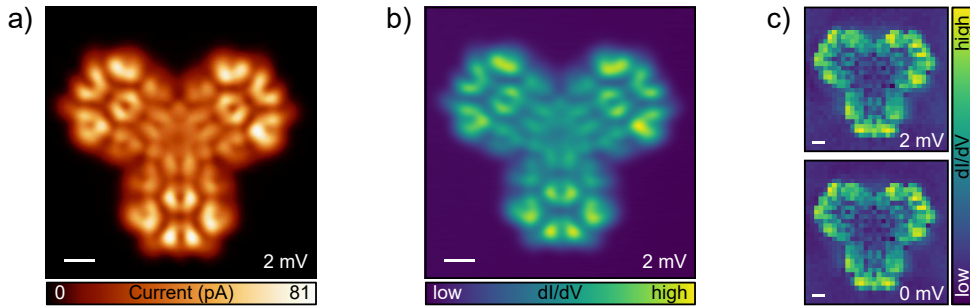


Figure S7. Constant-height a) current and b) conductance Kondo maps of **BAT**. c) Selected dI/dV maps at 2 mV and 0 mV extracted from the CITS of **BAT**. All maps are done with a CO tip. Scalebars: 4 Å.

G. IETS mapping of the spin excitation of AAT

We measured the derivative of the conductance from the second harmonic demodulated lock-in signal to map the molecular distribution of the spin excitation of **AAT**. The resulting maps match the simulations using the natural transition orbitals (NTO) from the two doublet states to the excited quartet state.

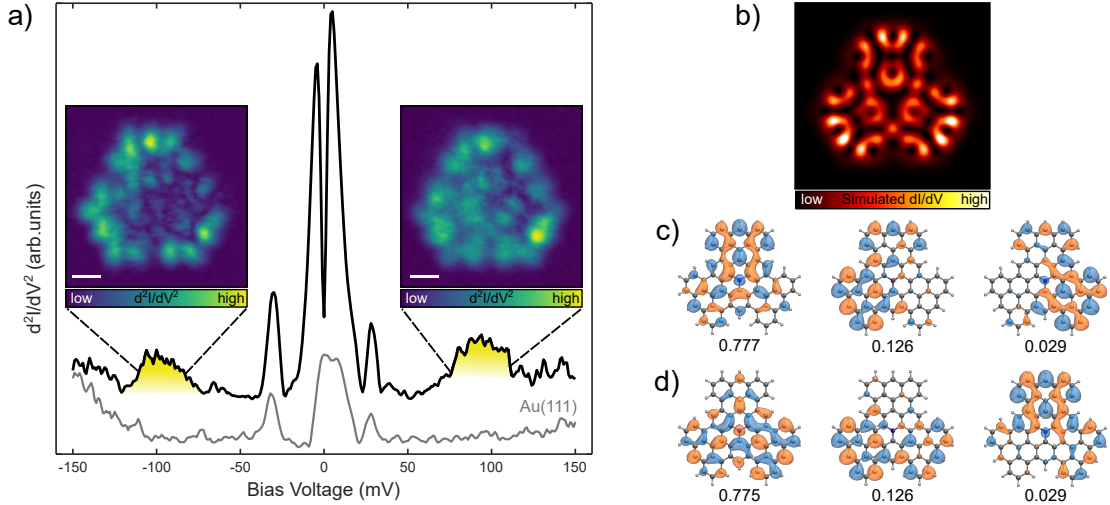


Figure S8. a) IETS spectra (d^2I/dV^2) measured over a zigzag edge of **AAT** (black) and on the bare surface (grey). The experimental spin excitation maps at ± 100 mV are shown as insets (scalebars 4 Å). b) Simulated dI/dV map obtained from the normalized weighted sum of the maps associated with each NTOs in c) and d). Corresponding NTOs with their eigenvalues from the c) first and d) second doublet state to the quartet state, computed with CASCI(11,11) from DFT orbitals.

H. Orbital mapping and Dyson orbitals

The experimentally mapped frontier orbitals in Fig. S9b and e match the computed Dyson orbitals in Fig. S9c and f, confirming the neutral character of the two molecules on the surface.

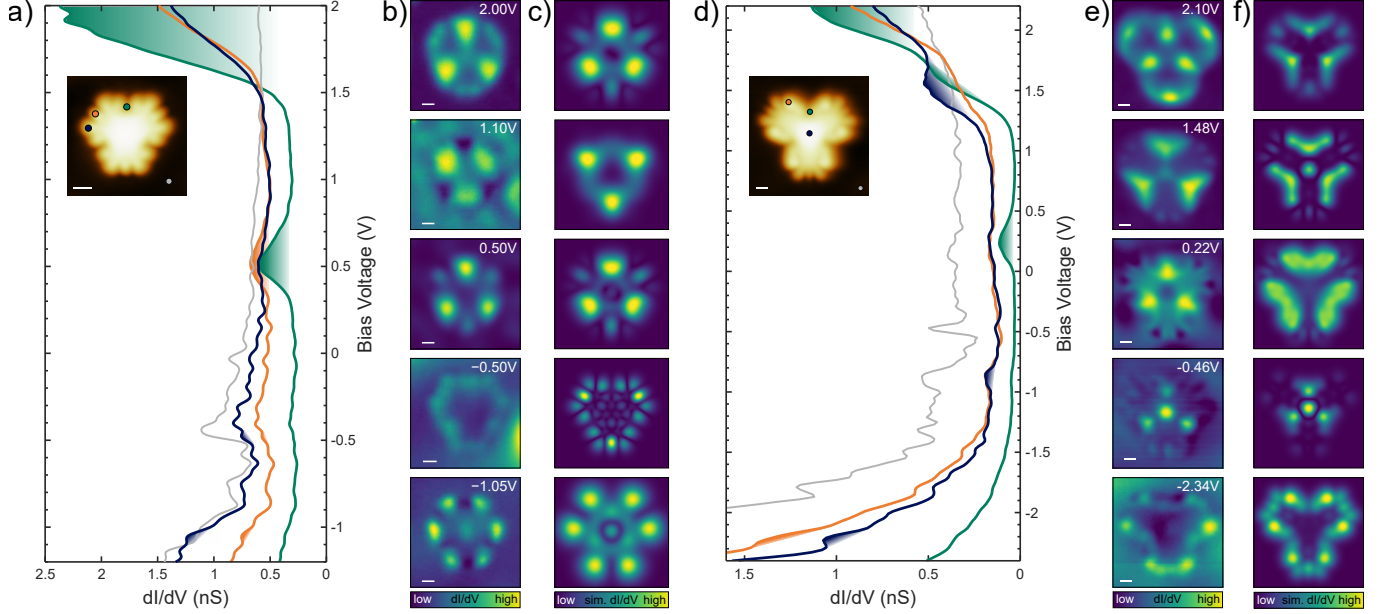


Figure S9. Long range STS spectra of a) **AAT** and d) **BAT** measured over several spots over the molecule and on the surface as marked by the colored dots in the STM image of the inset. Constant-current dI/dV maps of the frontier orbitals of b) **AAT** and e) **BAT**. Scalebars 4 Å. Simulated dI/dV maps of c) **AAT** and f) **BAT** obtained from the CASCI Dyson orbitals shown below.

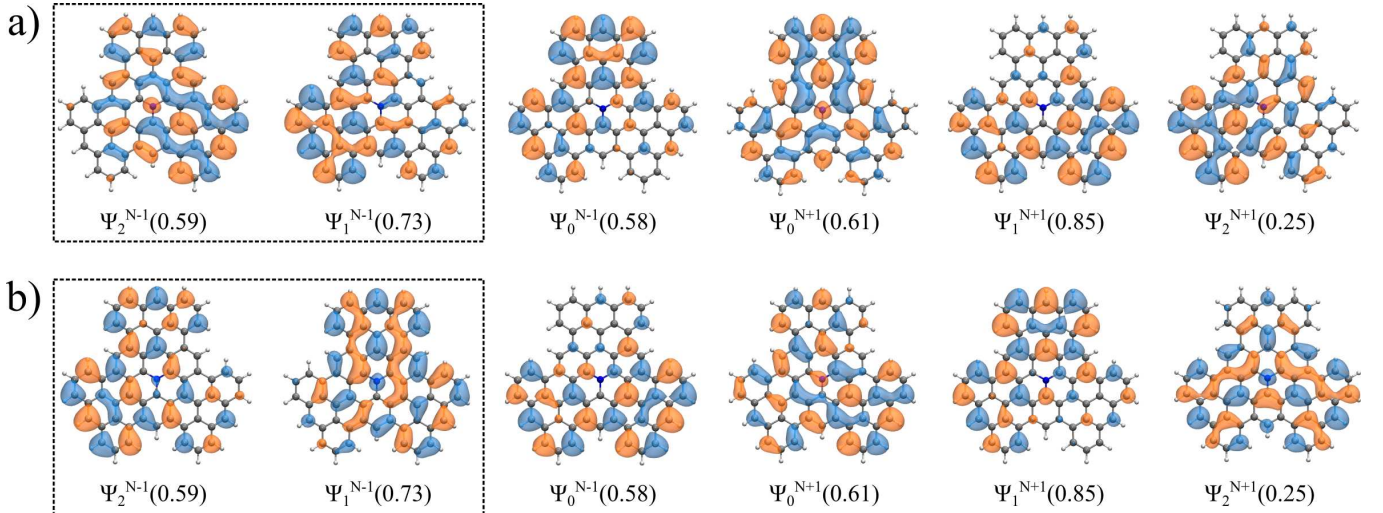


Figure S10. Dyson orbitals obtained from multireference CASCI calculations for the processes of single-electron addition and removal. The corresponding wavefunction norms are shown below for the **AAT**, using (a) the first doublet of the neutral state and (b) the second doublet of the neutral state. Orbitals highlighted with dashed boxes are degenerated.

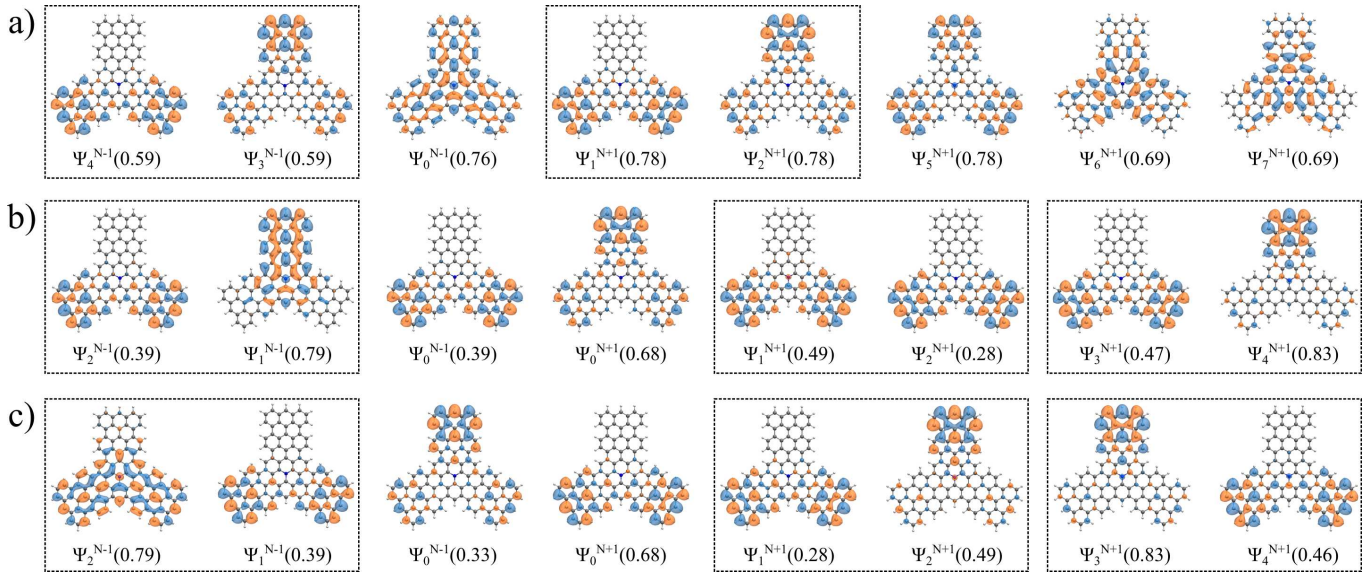


Figure S11. Dyson orbitals obtained from multireference CASCI calculations for the processes of single-electron addition and removal. The corresponding wavefunction norms are shown below for the **BAT**, using (a) the quartet of the neutral state, (b) the first doublet of the neutral state, and (c) the second doublet of the neutral state. Orbitals highlighted with dashed boxes are degenerated.

I. CASCI Calculations

Complete active space configuration interaction (CASCI) calculations were performed with an active space of 11 electrons in 11 orbitals, CAS(11,11), centered around the Fermi level. The orbitals included in the active space are shown in Figure S12(a,b) for **AAT** and **BAT**. The corresponding natural orbitals obtained from the ground-state CASCI calculation are presented in Figure S12(c,d) for **AAT** and **BAT**.

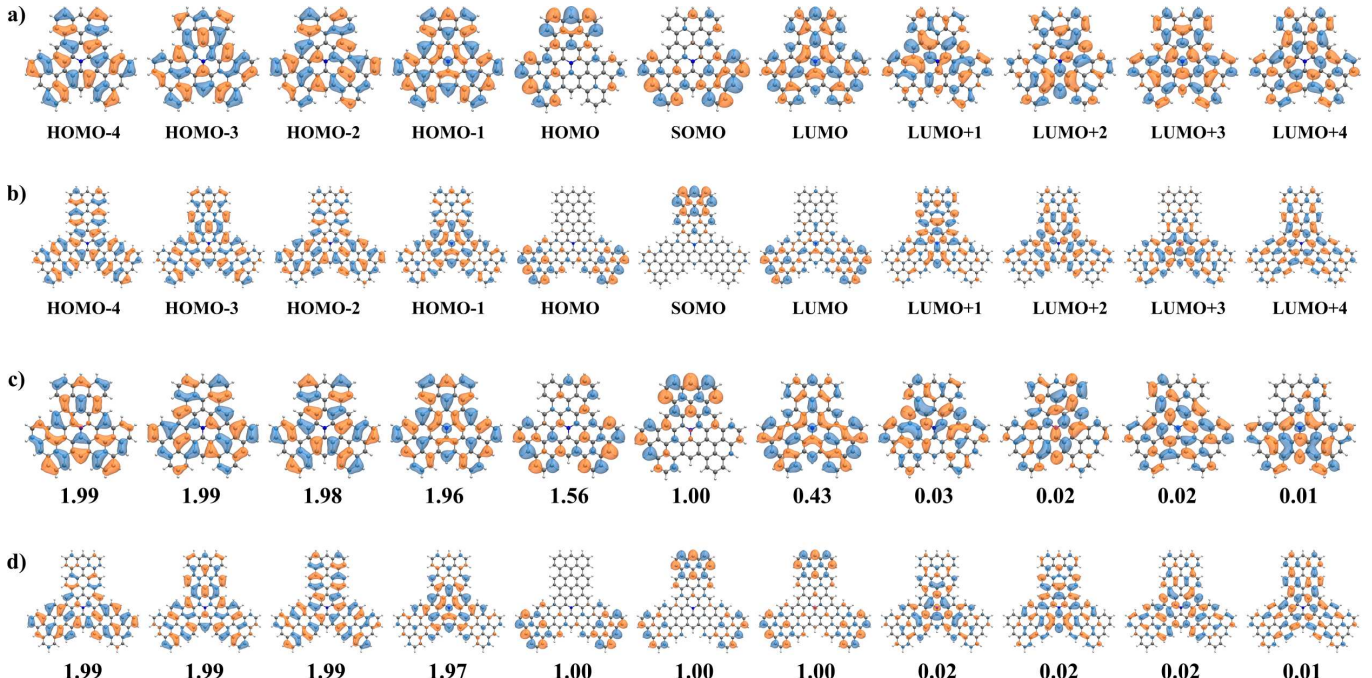


Figure S12. a) [b)] Restricted open-shell Kohn-Sham (ROKS) orbitals used for CASCI calculations for **AAT** [**BAT**]. c) [d)] Multireference natural orbitals from the CASCI ground state for **AAT** [**BAT**].

J. Kondo orbitals simulations

The spatial distribution of the Kondo resonance was theoretically investigated through Kondo orbital simulations based on a multi-channel Anderson model. The Hamiltonian was diagonalized considering the many-body multiplet structure derived from CASCI calculations for the neutral ground state and virtual charge states, following the methodology in Ref. [10]. Virtual processes involving the five lowest-energy multiplets in charged states were included to compute the scattering amplitudes.

For **AAT**, the analysis of coupling constants versus chemical potential (Figure S13a) identifies specific orbital channels with antiferromagnetic coupling ($j_a > 0$) that participate in the Kondo screening. The corresponding orbital isosurfaces at electron-hole symmetry (Fig. S13b) reveal the spatial patterns of these active channels for the first doublet state. Similar analysis for the second doublet state (Fig. S13c,d) shows distinct orbital participation in the screening process. As the ground state is doubly degenerated, consequently, the final Kondo spatial maps are constructed as a combination of the antiferromagnetic channels from both doublets.

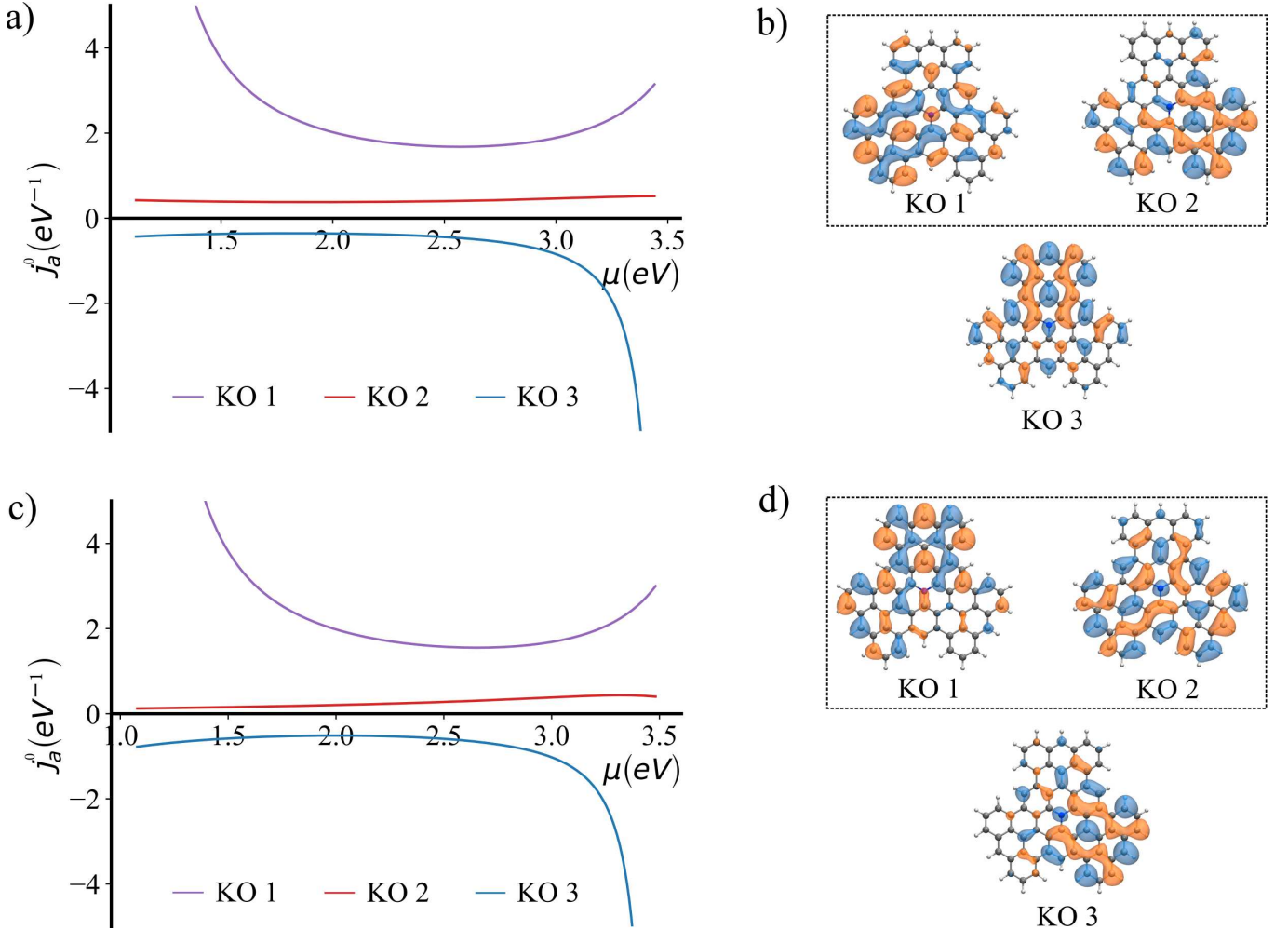


Figure S13. Results from the multi-orbital Kondo analysis used to simulate the spatial Kondo distribution map presented in the main text. (a) Coupling constants j_a as a function of chemical potential for each Kondo orbital (KO). (b) Orbital isosurfaces of the KOs that exhibit non-zero coupling to the substrate conduction electrons at the point of electron–hole symmetry. Orbitals highlighted with dashed boxes denote channels with antiferromagnetic coupling ($j_a > 0$) to the electron bath, and thus participate in the many-body Kondo screening process for the first doublet state. (c,d) Corresponding results for the second doublet state for **AAT**.

Similarly, for **BAT** molecule, the Kondo analysis provides the three antiferromagnetic coupling channels ($j_a > 0$) from the quartet state S14(a), while two antiferromagnetic channels from the first doublet and one antiferromagnetic channel from the second doublet. The CASCI calculations reveal a near-degeneracy between the lowest-lying quartet state and two doublet states. This near-degeneracy implies that the effective low-energy manifold cannot be described

by a single spin state, but instead arises from the interplay of the quartet and both doublets. As a result, the Kondo spatial distribution maps incorporate contributions from all three states.

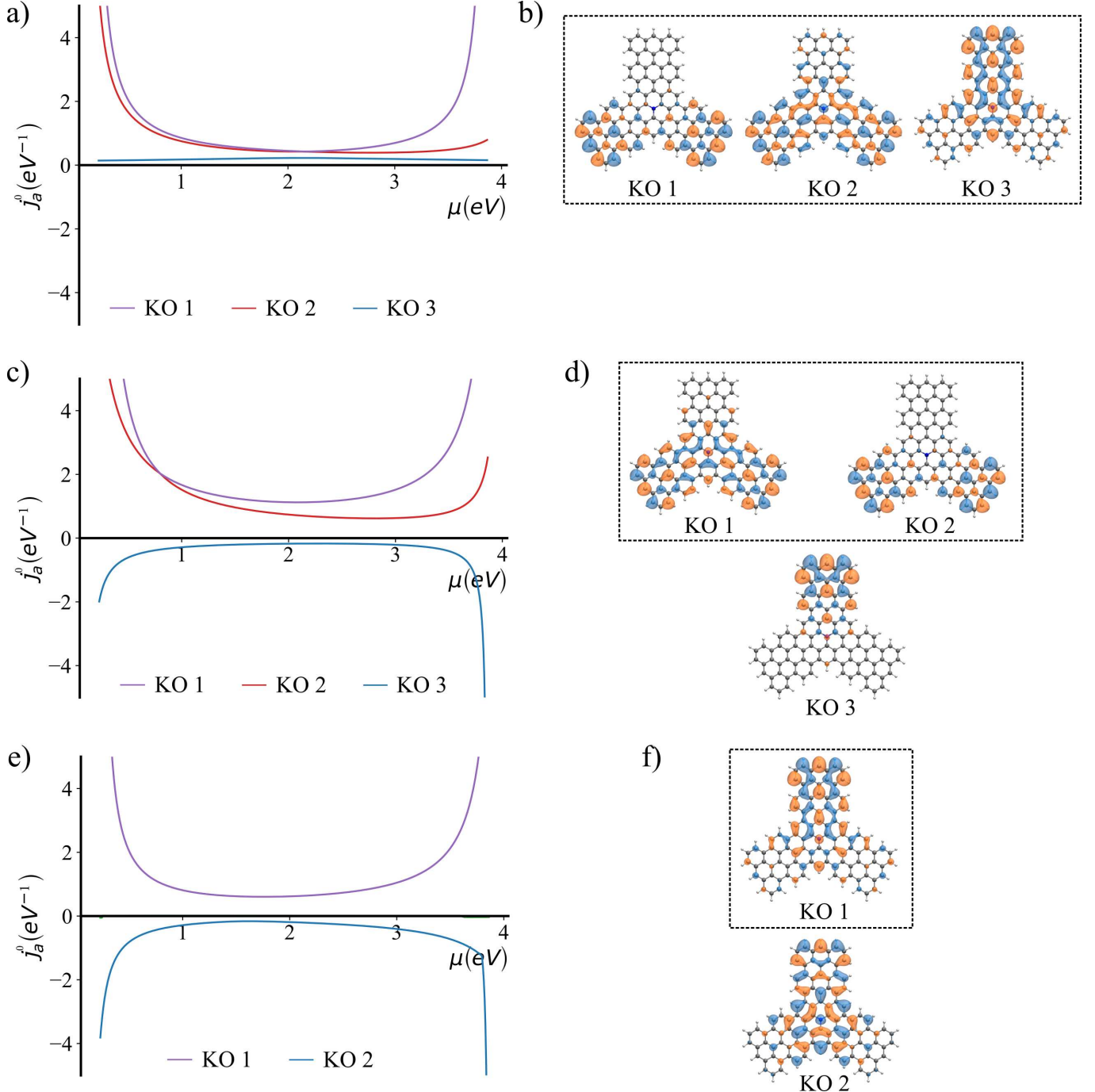


Figure S14. Results from the multi-orbital Kondo analysis used to simulate the spatial Kondo distribution map presented in the main text. (a) Coupling constants j_a as a function of chemical potential for each Kondo orbital (KO). (b) Orbital isosurfaces of the KOs that exhibit non-zero coupling to the substrate conduction electrons at the point of electron-hole symmetry. Orbitals highlighted with dashed boxes denote channels with antiferromagnetic coupling ($j_a > 0$) to the electron bath, and thus participate in the many-body Kondo screening process for the quartet state. (c,d) Corresponding results for the first doublet state, and (e,f) for the second doublet state for **BAT**.

K. CASSCF calculations

We computed the occupancies and energies of the natural orbitals in a CASSCF(9,11) model from optimized B3LYP def2-SVP def2/J RIJCOSX DFT orbitals using 10 roots and spins 5/2, 3/2 and 1/2 configurations for the four aza-platforms:

| NO | f | AT | | AAT | | BAT | | TAT | |
|----|-------------|--------|------|--------|------|--------|------|--------|---|
| | | E (eV) | f | E (eV) | f | E (eV) | f | E (eV) | f |
| 1 | 1.81 | -9.80 | 1.88 | -7.83 | 1.87 | -7.85 | 1.86 | -7.12 | |
| 2 | 1.77 | -8.92 | 1.87 | -8.05 | 1.84 | -7.23 | 1.84 | -7.14 | |
| 3 | 1.73 | -8.51 | 1.57 | -5.80 | 1.34 | -4.55 | 1.29 | -4.32 | |
| 4 | 1.05 | -3.07 | 1.04 | -3.04 | 1.03 | -3.00 | 1.00 | -2.96 | |
| 5 | 1.02 | -2.90 | 1.03 | -3.07 | 1.02 | -3.00 | 1.00 | -2.97 | |
| 6 | 0.61 | -0.02 | 0.79 | -1.96 | 0.95 | -2.77 | 0.99 | -2.94 | |
| 7 | 0.36 | 2.14 | 0.27 | 1.13 | 0.31 | 0.70 | 0.32 | 0.45 | |
| 8 | 0.30 | 2.68 | 0.19 | 1.31 | 0.29 | 0.55 | 0.31 | 0.33 | |
| 9 | 0.26 | 2.87 | 0.17 | 1.73 | 0.24 | 0.62 | 0.28 | 0.40 | |
| 10 | 0.05 | 6.36 | 0.12 | 1.55 | 0.08 | 1.88 | 0.07 | 1.20 | |
| 11 | 0.04 | 7.28 | 0.07 | 2.37 | 0.04 | 3.51 | 0.03 | 3.37 | |

Table I. Computed occupancies (f) and energies (E) for the natural orbitals (NO) obtained by CASSCF. The three orbitals in bold are the ones that contribute to the polypyridine character as the size of the molecule increases (plotted in Fig. 4c).

Fig. S15 shows the many-body spin states diagram obtained after a NEVPT2 correction [18]. In the case of **AT** in Fig. S15a, the two doublets are well separated in energy due to a Jahn-Teller distortion [19]. Each doublets are composed of a single spin multiplet, highlighting the monoradical nature of **AT**. In contrast, for **TAT** in Fig. S15d, the two doublet and quartet states are degenerated, indicating that **TAT** behaves as a non-interacting triradical molecule.

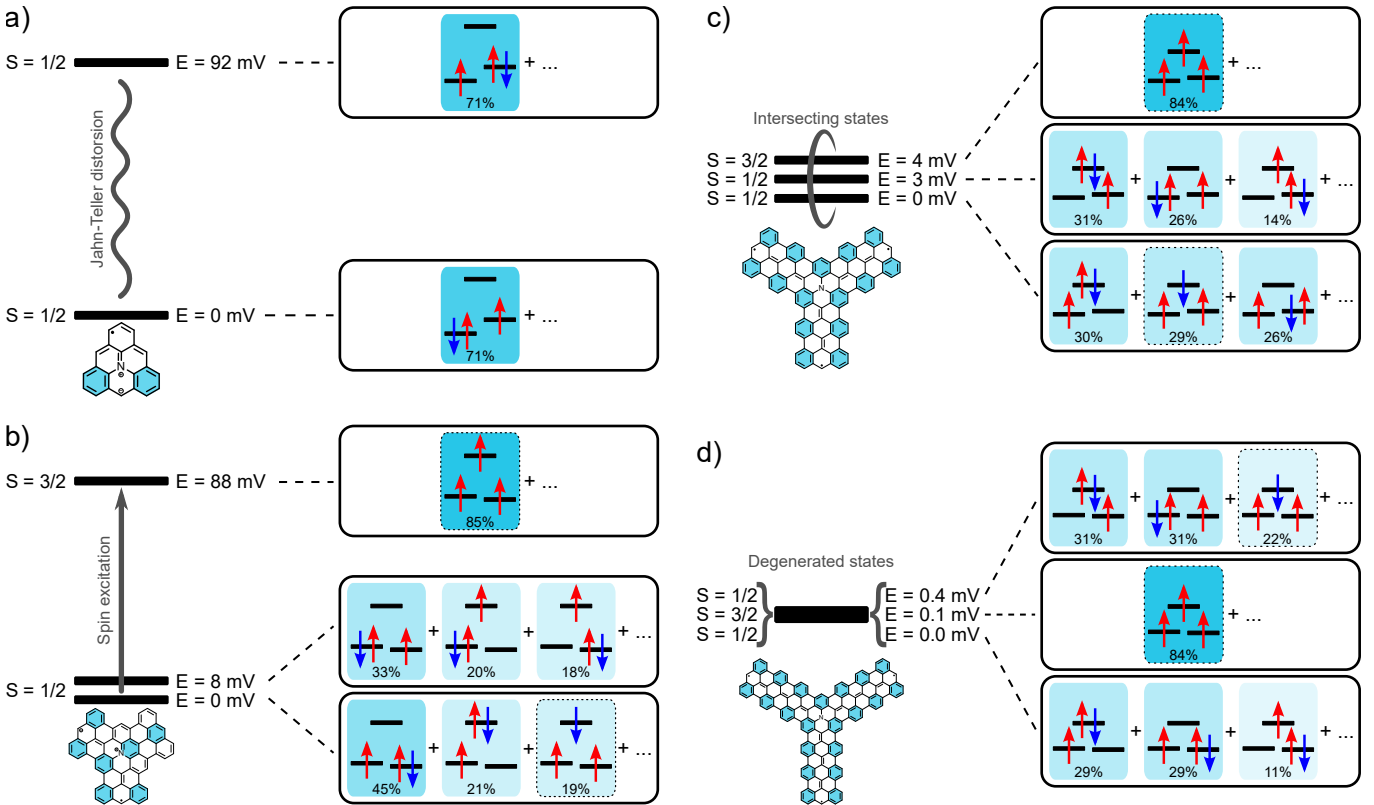


Figure S15. Many-body states diagram obtained from multi-reference calculations CASSCF NEVPT2 for a) **AT** a), b) **AAT**, c) **BAT**, and d) **TAT**. It shows the most important spin multiplets of the lowest energy states.

L. Hubbard toy-model

Here, we rationalize the magnetic exchange pattern in **BAT** using a four-site Hubbard model. Each site represents a topological zero-energy state (ZES), three of them at the termini of the 7AGNR extensions [20], and the forth one, at the junction among them [21]. Insets in Fig. S16 schematically show the model. The Hamiltonian reads

$$\mathcal{H} = -t \sum_{i=1,\sigma}^3 (c_{i,\sigma}^\dagger c_{0,\sigma} + \text{H.c.}) + U \sum_{i=0}^3 n_{i\uparrow} n_{i\downarrow} + \sum_{i=0,\sigma}^3 \epsilon_i n_{i,\sigma},$$

where the first term corresponds to electron hopping with amplitude t , the second to on-site Coulomb repulsion, and the third to the on-site energies ϵ_i , taken as zero except for the value of the central site that represents the aza core, ϵ_0 . The Hamiltonian was solved numerically by exact diagonalization, yielding the energies and total spin of the ground and excited states as a function of t for a representative value of on-site Coulomb repulsion $U = 2.5$ eV. To simulate the aza-core in **BAT**, we use a reduced on-site energy, $\epsilon_0 = -3$ eV, and consider only the subspace with five electrons ($N = 5$), while, for the all-carbon analogue, all on-site energies are set equal $\epsilon_0 = 0$ and $N = 4$.

Figures S16a and S16b show the results of the model for $N = 5$, $\epsilon_0 = -3$ eV, and for $N = 4$, $\epsilon_0 = 0$, representing the N-doped and all-carbon cases, respectively. In the former, the ground state is a doubly degenerate doublet, and the excitation energy to the lowest quartet state decreases monotonically with t , in agreement with our quantum-chemistry calculations. In this configuration, the three unpaired electrons at the edges form a frustrated spin trimer, with antiferromagnetic exchange mediated by the double occupancy of the aza-core. This exchange pattern reverses when the core becomes singly occupied, as in the all-carbon platform. In that case, the ground state is a high-spin triplet, described in this model as three ferromagnetically aligned terminal spins and a singly occupied junction state [21], antiferromagnetically coupled to them. The excitation energy to the two degenerate singlet states also decreases monotonically with the hopping parameter t .

These results show that the exchange pattern between the terminal spins is completely reversed by the N substitution because of the different occupation of the site at the center. This explains why the three terminal spins in **BAT** are AFM aligned, in spite of lying in the same sublattice. However, since the graphene lattice is not half occupied, this does not contradict Lieb's theorem [22].

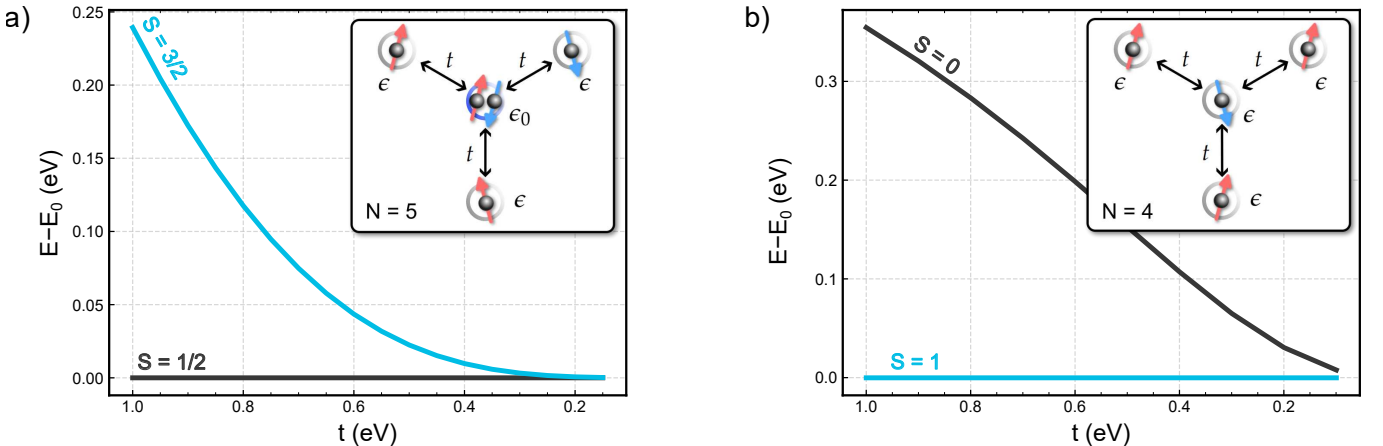


Figure S16. Difference in energy between the excited and ground states obtained from the four-site Hubbard toy model as a function of hopping parameter t for the case of (a) $\epsilon_0 = -3$ eV and $N = 5$, simulating an aza-junction, with an extra electron provided by the N-doping at the center, and (b) $\epsilon_0 = 0$ and $N = 4$, simulating the equivalent case with no doping. The results are computed with $U = 2.5$ eV. The exchange pattern is completely reversed by the N substitution. Schematic representations of each model with their approximate occupations are shown as insets.

M. CAS-Hubbard calculations

To complement the above calculations, we also consider an analysis of the excitation spectra based on the Hubbard Hamiltonian

$$H = \sum_{\langle ij \rangle, \sigma} h_{ij} c_{i\sigma}^\dagger c_{j\sigma} + U \sum_i n_{i\uparrow} n_{i\downarrow}, \quad (1)$$

where $n_{i\sigma} = c_{i\sigma}^\dagger c_{i\sigma}$ and $c_{i\sigma}$ are the electronic number and annihilation operators, respectively, corresponding to site i and spin σ . The matrix h_{ij} includes the onsite potentials ε_i along the diagonal and hopping matrix elements t_{ij} off the diagonal. U denotes the onsite Coulomb repulsion for the carbon $2p_z$ orbital. We include up to third-nearest neighbor hopping with $(t_1, t_2, t_3) = -(2.7, 0.2, 0.18)$ eV following a parametrization for graphene nanoribbons from Ref. [23]. For the electrostatic potential associated with the nitrogen atom we assume a Gaussian variation in the onsite energies $\varepsilon_i(\rho) = \varepsilon_N e^{-(\rho/R)^2}$ a distance ρ away from the central heteroatom. Here $\varepsilon_N = -5.5$ eV and $R = 1.5$ Å are *effective* model parameters that characterize the depth and extension of the potential variation, respectively, with values chosen to provide the best fit to the excitation energies seen experimentally (~ 100 meV for AAT and ~ 0 meV for BAT and TAT).

The Hubbard Hamiltonian may also be expressed in the eigenbasis $(\varepsilon_\alpha, \phi_\alpha)$ of h_{ij} as

$$H = \sum_{\alpha\sigma} \varepsilon_\alpha n_{\alpha\sigma} + U \sum_{\alpha\alpha'\beta\beta'} \left(\sum_i \phi_{\alpha_i}^* \phi_{\alpha'_i} \phi_{\beta_i}^* \phi_{\beta'_i} \right) c_{\alpha\uparrow}^\dagger c_{\alpha'\uparrow} c_{\beta\downarrow}^\dagger c_{\beta'\downarrow}. \quad (2)$$

In this basis we explore the many-body energy spectrum with the complete active space (CAS) method, considering the active space $\text{CAS}(N_{\text{elec}}, N_{\text{orb}})$ for the number of included electrons and orbitals, respectively. The active orbitals are chosen around the singly-occupied molecular orbital (SOMO). For describing the low-energy states of the present molecular systems based on the Hubbard Hamiltonian, we find it to be sufficient to consider just three electrons in the first three frontier orbitals, i.e., CAS(3,3) as shown in Fig. S17. The accuracy of this minimal approach is bench-marked by increasing the active space to both CAS(5,4) and CAS(11,10), providing minimal changes to the excitation spectrum.

As shown in Fig. S18 we also explored the all-carbon analogues of the different molecules. Here the minimal model corresponds to CAS(2,3). However, for the larger molecules, it is necessary to include more orbitals in the active space for an accurate description of the first excitation gap.

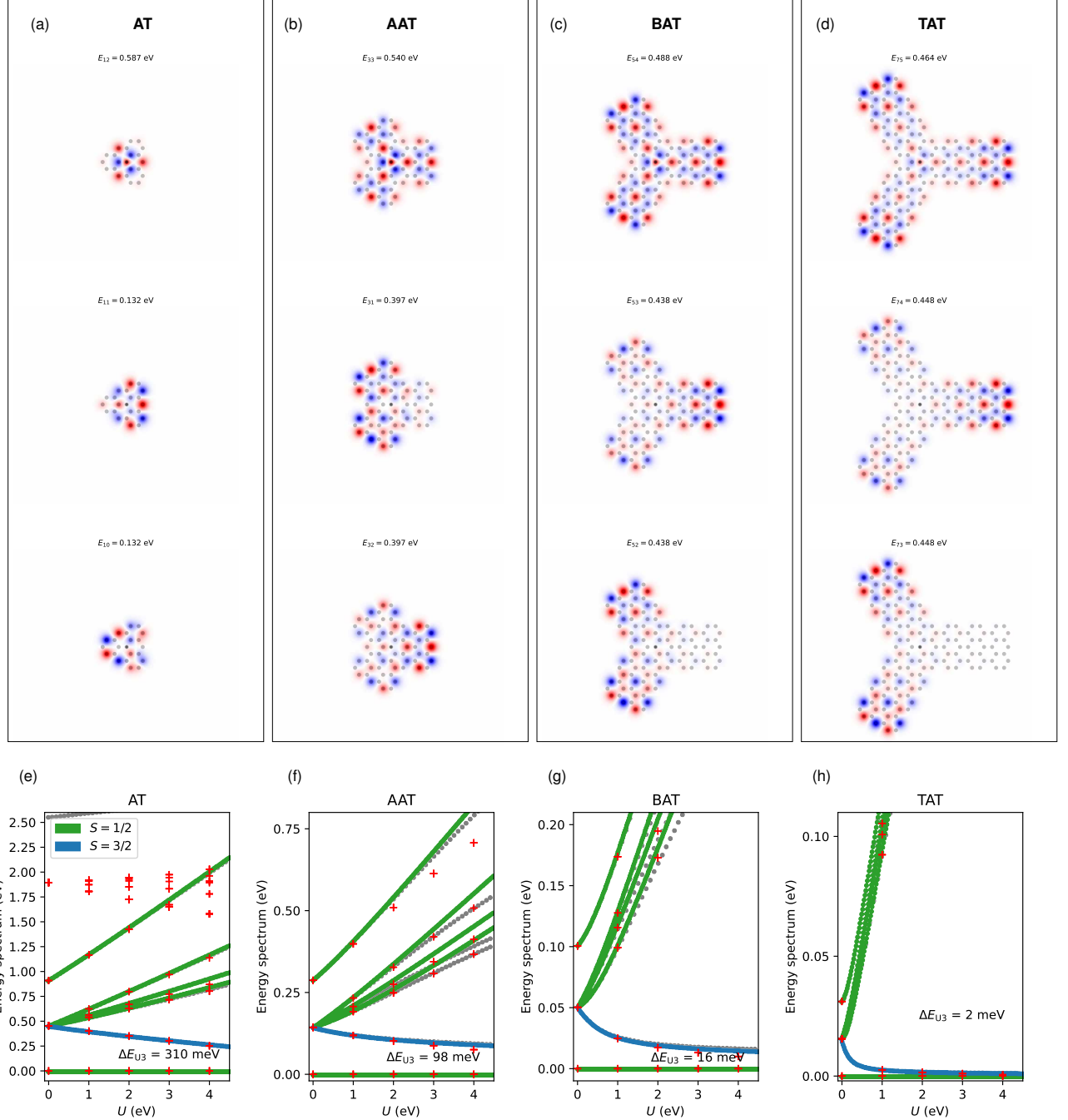


Figure S17. (a)-(d) Visualization of the active orbitals as included in CAS(3,3) with the Hubbard Hamiltonian. The sign and real-space intensity is shown with a red/blue colormap. The gray dots indicate the atomic positions. The first pair of orbitals (lower two rows) are degenerate and have no weight on the central nitrogen atom. In contrast, the third orbital (top row) is nondegenerate and has weight on nitrogen. (e)-(h) Calculated energy spectrum. The green/blue dots correspond to the minimal CAS(3,3) description. The gray dots [red crosses] correspond to more accurate CAS(5,4) [CAS(11,10)] calculations, essentially providing the same result for the low-energy states. The label ΔE_{U3} indicates the excitation gap at the CAS(3,3) level at $U = 3$ eV.

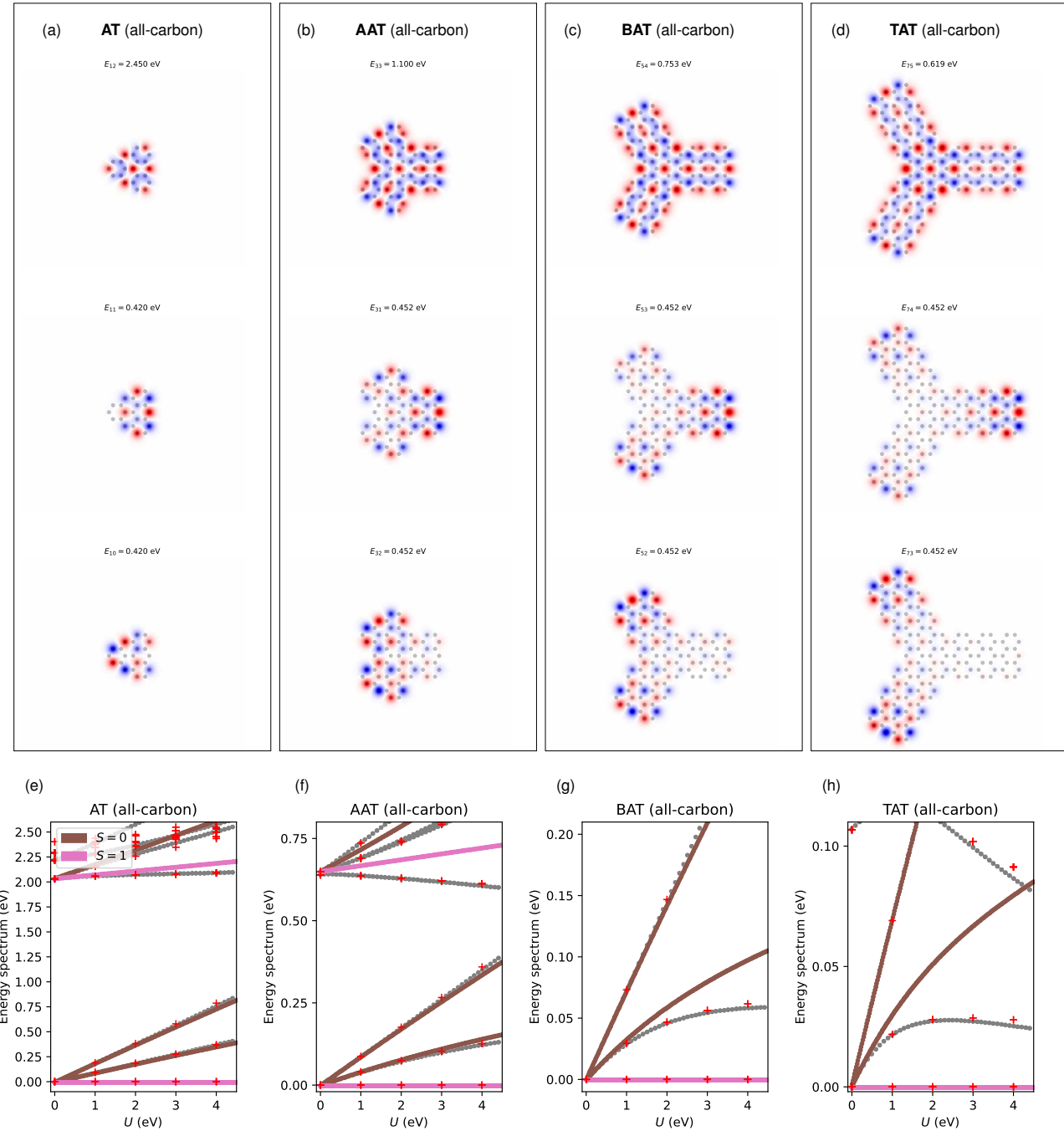


Figure S18. (a)-(d) Visualization of the active orbitals as included in CAS(2,3) with the Hubbard Hamiltonian for the all-carbon cases of Fig. S17. (e)-(h) Calculated energy spectrum. The brown/pink dots correspond to the minimal CAS(2,3) description. The gray dots [red crosses] correspond to more accurate CAS(4,4) [CAS(10,10)] calculations. For BAT and TAT, CAS(2,3) significantly overestimates the first excitation gap.

[1] I. Horcas, R. Fernández, J. M. Gómez-Rodríguez, J. Colchero, J. Gómez-Herrero, and A. M. Baro, WSXM: A software for scanning probe microscopy and a tool for nanotechnology, *Review of Scientific Instruments* **78**, 013705 (2007).

[2] E. Turco, M. Aapro, S. C. Ganguli, N. Krane, R. Drost, N. Sobrino, A. Bernhardt, M. Juríček, R. Fasel, P. Ruffieux, P. Liljeroth, and D. Jacob, Demonstrating Kondo behavior by temperature-dependent scanning tunneling spectroscopy, *Physical Review Research* **6**, L022061 (2024).

[3] V. Blum, R. Gehrke, F. Hanke, P. Havu, V. Havu, X. Ren, K. Reuter, and M. Scheffler, Ab initio molecular simulations with numeric atom-centered orbitals, *Computer Physics Communication* **180**, 2175 (2009).

[4] C. Adamo, M. Cossi, and V. Barone, An accurate density functional method for the study of magnetic properties: the pbe0 model, *Journal of Molecular Structure: THEOCHEM* **493**, 145 (1999).

[5] I. Neese, The ORCA program system, *WIREs Computational Molecular Science* **2**, 73 (2012).

[6] R. L. Martin, Natural transition orbitals, *The Journal of Chemical Physics* **118**, 4775 (2003).

[7] J. V. Ortiz, Dyson-orbital concepts for description of electrons in molecules, *The Journal of Chemical Physics* **153**, 070902 (2020).

[8] M. Kumar, D. Soler-Polo, M. Lozano, E. Monino, L. Veis, and P. Jelinek, Multireference Theory of Scanning Tunneling Spectroscopy Beyond One-Electron Molecular Orbitals: Can We Image Molecular Orbitals?, *Journal of the American Chemical Society* **147**, 24993 (2025).

[9] R. Zuzak, M. Kumar, O. Stoica, D. Soler-Polo, J. Brabec, K. Pernal, L. Veis, R. Blieck, A. M. Echavarren, P. Jelinek, and S. Godlewski, On-Surface Synthesis and Determination of the Open-Shell Singlet Ground State of Tridecacene**, *Angewandte Chemie International Edition* **63**, e202317091 (2024).

[10] A. Calvo-Fernández, M. Kumar, D. Soler-Polo, A. Eiguren, M. Blanco-Rey, and P. Jelínek, Theoretical model for multi-orbital Kondo screening in strongly correlated molecules with several unpaired electrons, *Physical Review B* **110**, 165113 (2024).

[11] O. Krejčí, P. Hapala, M. Ondráček, and P. Jelínek, Principles and simulations of high-resolution STM imaging with a flexible tip apex, *Physical Review B* **95**, 045407 (2017).

[12] M. Vilas-Varela, F. Romero-Lara, A. Vegliante, J. P. Calupitan, A. Martínez, L. Meyer, U. Uriarte-Amiano, N. Friedrich, D. Wang, F. Schulz, N. E. Koval, M. E. Sandoval-Salinas, D. Casanova, M. Corso, E. Artacho, D. Peña, and J. I. Pascual, On-Surface Synthesis and Characterization of a High-Spin Aza-[5]-Triangulene, *Angewandte Chemie International Edition* **62**, e202307884 (2023).

[13] L. M. Mateo, Q. Sun, S.-X. Liu, J. J. Bergkamp, K. Eimre, C. A. Pignedoli, P. Ruffieux, S. Decurtins, G. Bottari, R. Fasel, and T. Torres, On-Surface Synthesis and Characterization of Triply Fused Porphyrin–Graphene Nanoribbon Hybrids, *Angewandte Chemie International Edition* **59**, 1334 (2020).

[14] M. R. Ajayakumar, J. Ma, and X. Feng, π -Extended peri-Acenes: Recent Progress in Synthesis and Characterization, *European Journal of Organic Chemistry* **2022**, e202101428 (2022).

[15] G. Trinquier and J.-P. Malrieu, Predicting the Open-Shell Character of Polycyclic Hydrocarbons in Terms of Clar Sextets, *The Journal of Physical Chemistry A* **122**, 1088 (2018).

[16] D. G. de Oteyza and T. Frederiksen, Carbon-based nanostructures as a versatile platform for tunable π -magnetism, *Journal of Physics: Condensed Matter* **34**, 443001 (2022).

[17] D. Jacob, Temperature evolution of the Kondo peak beyond Fermi liquid theory, *Physical Review B* **108**, L161109 (2023).

[18] C. Angeli, M. Pastore, and R. Cimiraglia, New perspectives in multireference perturbation theory: The n-electron valence state approach, *Theoretical Chemistry Accounts* **117**, 743 (2007).

[19] M. E. Sandoval-Salinas, A. Carreras, and D. Casanova, Triangular graphene nanofragments: Open-shell character and doping, *Physical Chemistry Chemical Physics* **21**, 9069 (2019).

[20] T. Cao, F. Zhao, and S. G. Louie, Topological Phases in Graphene Nanoribbons: Junction States, Spin Centers, and Quantum Spin Chains, *Physical Review Letters* **119**, 076401 (2017).

[21] G. Tamaki, T. Kawakami, and M. Koshino, Topological junction states and their crystalline network in systems with chiral symmetry: Application to graphene nanoribbons, *Physical Review B* **101**, 205311 (2020).

[22] E. H. Lieb, Two theorems on the Hubbard model, *Physical Review Letters* **62**, 1201 (1989).

[23] Y. Hancock, A. Uppstu, K. Saloranta, A. Harju, and M. J. Puska, Generalized tight-binding transport model for graphene nanoribbon-based systems, *Phys. Rev. B* **81**, 245402 (2010).